Modeling Carbon Dioxide Hydrate Particle Releases in the Deep Ocean

by

Eric J. Wannamaker

Submitted to the Department of Civil and Environmental Engineering
in partial fulfillment of the requirements for the degree of

Master of Science in Civil and Environmental Engineering

at the

MASSACHUSETTS INSTITUTE OF TECHNOLOGY

June 2002

© Massachusetts Institute of Technology 2002. All rights reserved.

Author . . . .
Department of Civil and Environmental Engineering
May 17, 2002

Certified by . . . .
E. Eric Adams
Senior Research Engineer
Thesis Supervisor

Accepted by . . . .
Oral Buyukozturk
Chairman, Departmental Committee on Graduate Studies

Modeling Carbon Dioxide Hydrate Particle Releases in the Deep Ocean

by

Eric J. Wannamaker

Submitted to the Department of Civil and Environmental Engineering
on May 17, 2002, in partial fulfillment of the
requirements for the degree of
Master of Science in Civil and Environmental Engineering

Abstract

This work investigates the environmental impacts of releasing solid CO_2 hydrate particles into the deep ocean for the purpose of CO_2 sequestration. Release of CO_2 in this form may be desirable as hydrate particles are negatively buoyant in seawater, and dissolution of CO_2 enhances this negative buoyancy via the solute density effect. Hence, the total plume thickness of a negatively buoyant CO_2 hydrate plume may exceed that of positively buoyant CO_2 release. This is seen as a potential advantage both in terms of dilution and sequestration depth.

A brief description of the two-phase integral plume model used for stagnant plume modeling is given as well as some background in multi-phase plume physics. Physical and chemical properties relevant to CO_2 hydrates and the ocean environment are discussed, as well as a description of the applicable carbonate chemistry. The integral model used for plume modeling is calibrated based on available data, as is the mass transfer model. The impact of mean particle size particle size distribution, and mass injection rate on relevant integrated parameters is explored via numerical modeling. A brief comparison of the plume group effect for positive and negative buoyancy is presented as well. Three different CO_2 release scenarios, including a hydrate particle plume, a towed pipe release, and a manifold based liquid CO_2 release are compared in terms of their pH impact to the water column.

Thesis Supervisor: E. Eric Adams
Title: Senior Research Engineer

Acknowledgments

Financial support from a National Science Foundation graduate research fellowship is gratefully acknowledged. Additional support was provided by the Ocean Carbon Sequestration Program, Biological and Environmental Research (BER), U. S. Dept. of Energy (grant number DE-FG02-01ER63078) and by the National Energy Technology Laboratory, U.S. Dept. of Energy (grant number DE-FG26-98FT40334).

I would like to thank two previous members of the Adams research group for helping me along. Brian Crounse, for writing the integral plume model and helping me with model related questions. Scott Socolofsky, for his tremendous help with any computer related problems and providing most of the data for model calibration. I'd also like to thank my thesis advisor, Eric Adams, for making my time at MIT rewarding. Whether it was providing me with the opportunity to travel to conferences and technical meetings, or patiently providing technical and career advice, Eric enabled me to get the most out of my education at MIT.

Finally, I'd like to thank my family and friends for their continued support, and especially Kara for always believing in me.

Contents

1 Introduction **15**

1.1 Carbon Sequestration 15

1.2 Two-phase plumes 16

1.3 Description of Numerical Model 18

1.3.1 Integral Models 18

1.3.2 Model Control Volume and Fluxes 19

1.3.3 Model Implementation 20

1.4 Goals of this Work 21

2 Chemical and Physical Properties **23**

2.1 CO_2 Hydrates 23

2.1.1 Formation 23

2.1.2 Mass Transfer 25

2.1.3 Particle Size Distribution 28

2.1.4 Particle Slip Velocity 29

2.2 Carbonate Chemistry 29

2.2.1 CO_2 in water 29

2.2.2 pH calculations 32

2.3 Seawater 35

3 Model Validation **37**

3.1 Trap Height and Volume Fluxes 37

3.1.1 Trap Height 38

3.1.2 Volume Fluxes 39
3.2 Buoyant Detrainment 43
3.3 Model Functionality 46
3.4 Mass Transfer 48

4 Modeling Results **51**
4.1 Particle Size Distribution 51
4.1.1 Release Conditions 51
4.1.2 Plume Characteristics 52
4.1.3 Averaged Quantities 56
4.2 Particle Diameter and Mass Flux 59
4.2.1 Release Conditions 59
4.2.2 Plume Depth 60
4.2.3 DIC and pH 60
4.2.4 Sensitivity to Mass Transfer Model 63
4.2.5 Implications of Ambient Current 64
4.2.6 Comparison of Positive and Negative Buoyancy 68

5 Comparison of Release Scenarios **73**
5.1 Hydrate Particle Plume 74
5.1.1 Undissolved Mass Reaching Sea Floor 77
5.2 Ship-based Release 79
5.3 Bottom Manifold Release 82
5.4 Summary 84
5.4.1 Importance of Lateral Diffusion 86
5.4.2 Sensitivity to Design Variables 87

6 Conclusions **89**
6.1 Summary 89
6.2 Conclusions 90
6.3 Recommendations for Further Study 91

List of Figures

1-1 Schematic of particle plume and related parameters. 17

1-2 Two phase plume types. 18

1-3 Integral Model Control Volume. 19

2-1 Phase Diagram for CO_2 in the presence of water. 24

2-2 Typical gas clathrate hydrate structures. 24

2-3 CO_2 hydrate forming nozzle. 25

2-4 Falling, isolated hydrate particle dissolution for different initial diameters. . . 29

2-5 Example particle size distributions. 30

2-6 Profiles of DIC, $C - alk$, and pH. 31

2-7 Comparison of CO_2 solubility and DIC as a function of depth 32

2-8 Ambient Density profile from Station Aloha 36

3-1 Schematic of plume fluxes. 38

3-2 Comparison of modeled plume heights with experimental data. 40

3-3 Comparison of modeled first peel volume fluxes with experimental data. . . . 42

3-4 Comparison of modeled first peel intrusion flux with experimental data. . . . 42

3-5 Definition of fluxes for peeling flux, f, calculation. 43

3-6 Model predicted f vs. ϵ for $U_N = 1.5$. 44

3-7 Model predicted f vs. ϵ curves for various U_N, with superimposed experimental values. 45

3-8 Model predicted f for different ϵ, plotted alongside experimental data. 45

3-9 Comparison of plume model output for equal but opposite buoyancy fluxes. . 47

3-10 Comparison of mass transfer correlation with experimental data 50

4-1 Discrete mass fraction by radius. 52
4-2 Plume width vs. depth for different particle distributions. 53
4-3 Volume flux vs. depth for different particle distributions. 54
4-4 CO_2 hydrate mass flux vs. depth for different particle distributions. 54
4-5 CO_2 hydrate mass flux vs. radius at various depths for different initial particle size distributions 55
4-6 Characteristic plume depths for various particle size distributions. 56
4-7 Average DIC and pH drop for plume water intruding into ambient for different particle size distributions. 57
4-8 Equivalent flux of dispersed CO_2 reaching sea-floor for different particle size distributions. 58
4-9 Plume depth and average intrusion depth vs. particle diameter for different CO_2 release rates. 61
4-10 Undissolved mass reaching bottom of domain vs. particle diameter for different CO_2 release rates. 61
4-11 Average intruding additional DIC and pH vs. particle diameter for different CO_2 release rates. 62
4-12 Far-field (1000m downstream) additional DIC and pH vs. particle diameter for different CO_2 release rates. 64
4-13 Sensitivity of plume depths to mass transfer model. 65
4-14 Sensitivity of average DIC and pH drop to mass transfer model. 65
4-15 Sensitivity of undissolved mass reaching bottom to mass transfer model. . . . 66
4-16 Schematic of a two-phase plume in a crossflow. 66
4-17 Comparison of trap and separation heights for modeled fluxes and diameters. 68
4-18 Linear stratification profile for buoyancy comparison runs. 69
4-19 Comparison of plume and single particle distances for buoyancy comparison runs. 71

5-1 Schematic of a hydrate particle release. 75

5-2 pH drop traveling downstream from a hydrate plume as a function of time. . 76
5-3 Volume of water at different pH drop ranges produced by a hydrate plume. . 77
5-4 Average pH drop traveling downstream from a CO_2 hydrate mound as a function of time. 79
5-5 Schematic of a ship based release. 80
5-6 pH drop traveling away from a towed pipe as a function of time. 81
5-7 Volume of water at different pH drop ranges produced by a towed pipe. . . . 82
5-8 Schematic of a sea-floor manifold release. 83
5-9 pH drop traveling away from a liquid CO_2 manifold as a function of time. . . 85
5-10 pH drop traveling away from different CO_2 releases as a function of time. . . 85
5-11 Volume of water at different pH drop ranges produced by different CO_2 releases. 86

List of Tables

3.1 Trap and Peel height data. 39
3.2 Volume flux data. 41
3.3 Model Parameters for basic functionality verification. 46

4.1 U_N for modeled release parameters. 59

5.1 Options for Ocean CO_2 injection. 73

Chapter 1

Introduction

1.1 Carbon Sequestration

Global atmospheric CO_2 concentration has been on the rise since the industrial revolution due to increased fossil fuel combustion. High atmospheric concentrations of CO_2, a so-called greenhouse gas, are raising concerns about possible global climate change. Carbon sequestration in the ocean has been proposed as a strategy for reducing global atmospheric CO_2 concentrations in the near term. CO_2 sequestration in the ocean is proposed only as method to reduce peak atmospheric CO_2 concentration, and to lessen the rate of increase in concentration, since the concentration of CO_2 in the ocean and in the atmosphere will eventually reach equilibrium. (Herzog et al. 2001).

Coal-fired power plants are a logical starting point for CO_2 sequestration. Not only do they represent a significant portion of CO_2 emissions, their flue gases contain CO_2 in relative purity. CO_2 could be isolated from the power plant exhausts then injected into the ocean in a variety of chemical forms. One way to divide the potential forms of CO_2 is in terms of their buoyancy relative to seawater.

The positively buoyant forms of CO_2 in the ocean are either as a liquid at ambient ocean temperature and below about 400 meter depth, or as a gas at ambient temperatures above 400 meters. Since it is desirable to sequester CO_2 deep in the ocean, gaseous CO_2 has not been considered a release option. However, there has been a host of work on positively buoyant liquid CO_2 releases in the deep ocean. Liquid CO_2 could be released from a manifold at depth of around 800m, where it would form an ascending droplet plume. The main disadvantage of a positively buoyant release is that the sequestration depth is compromised by plume travel.

There are many different ways to obtain CO_2 in a negatively buoyant form. Dry ice (Nakashiki et al. 1994, Caulfield 1996) and very cold liquid CO_2 (Aya et al. 1999) are negatively buoyant phases of pure CO_2. CO_2 can be reacted to form dense $CaCO_3$ slurries (Rau & Caldeira 1999, Caldeira & Rau 2000), or put into a $CaCO_3$ emulsion (Golomb & Angelopoulos 2001). A highly concentrated CO_2 and seawater solution is negatively buoyant, and may be used to induce a gravity current (Haugen & Drange 1992, Adams et al. 1995, Adams et al. 1997, Saito et al. 2000). At depths below 500m, CO_2 will form a negatively buoyant clathrate hydrate (Holder et al. 2001), which is the focus of this study. Negatively buoyant releases are advantageous because the sequestration depth will be deeper than the release depth, and, in the case of plume-type releases, there is a positive feedback in the sense that the dissolving CO_2 makes the plume water more dense.

1.2 Two-phase plumes

A two-phase plume is formed when a continuous release of a dispersed, immiscible, buoyant substance is introduced into a medium such as water. Typical uses of such plumes include reservoir de-stratification with air bubbles, aeration, and dredged sediment disposal. CO_2 droplet or hydrate particle plumes are a special case in that the dispersed phase dissolves as the plume develops, and modifies the plume water buoyancy via the solute density effect. The evolution of a CO_2 hydrate particle plume in ambient stratification proceeds as follows.

At the release point, the negatively buoyant CO_2 hydrate particles begin to descend and create turbulence in the ambient fluid. This turbulence induces entrainment of fluid from the ambient. Due to stratification, as the plume water travels along with the particles it becomes increasingly positively buoyant in comparison to the ambient, although the negative buoyancy induced by particle dissolution slightly counteracts this effect. Eventually, however, the positive buoyancy of the plume water can no longer be supported by the particles, and the plume water detrains, or 'peels' away from the descending particles. This detrained

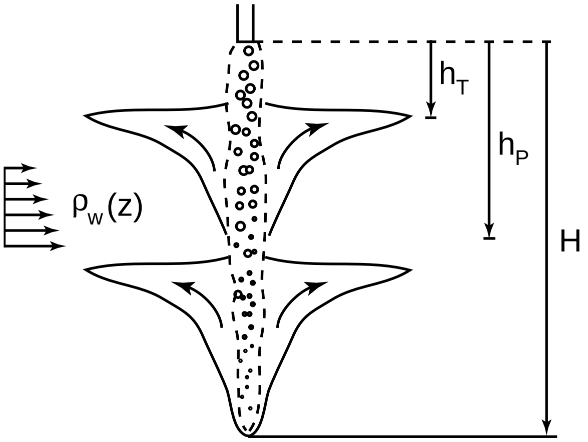

Figure 1-1: Schematic of particle plume and related parameters.

water is lighter than the ambient, and so ascends to a point of neutral buoyancy where it forms an intrusion. Figure 1-1 shows a schematic of this behavior.

Also shown in Figure 1-1 are some important parameters associated with two-phase plumes. The plume shown has two distinct peeling events. H is the total plume depth, or the depth at which all of the particles have dissolved and the plume momentum is zero. h_T is the depth at which the intruded water from the first peel is trapped, or neutrally buoyant. h_p is the depth at which the first peel occurs. $\rho_w(z)$ indicates the ambient density stratification. The characteristic plume depths mentioned above, as well as plume peeling behavior, are functions of the amount and type of particles released.

Socolofsky (2001) determined that a single dimensionless number, U_N, describes plume type for two-phase plumes in deep water. U_N is defined as

$$U_N = \frac{u_s}{(BN)^{1/4}} \tag{1.1}$$

where u_s is the particle slip velocity (a function of diameter), $B = gQ_p(\rho - \rho_p)/\rho$ is the buoyancy flux, Q_p is the volume flux of particles, ρ_p is the particle density, ρ is the ambient density, and $N = [-(g/\rho)(\partial\rho/\partial z)]^{1/2}$ is the Brunt-Vaisälä buoyancy frequency. Figure 1-2 illustrates how plume behavior changes with increasing U_N, and the plume type classification adopted by Socolofsky. In Type 1* plumes, for U_N of zero to about 1.5, some of the particles

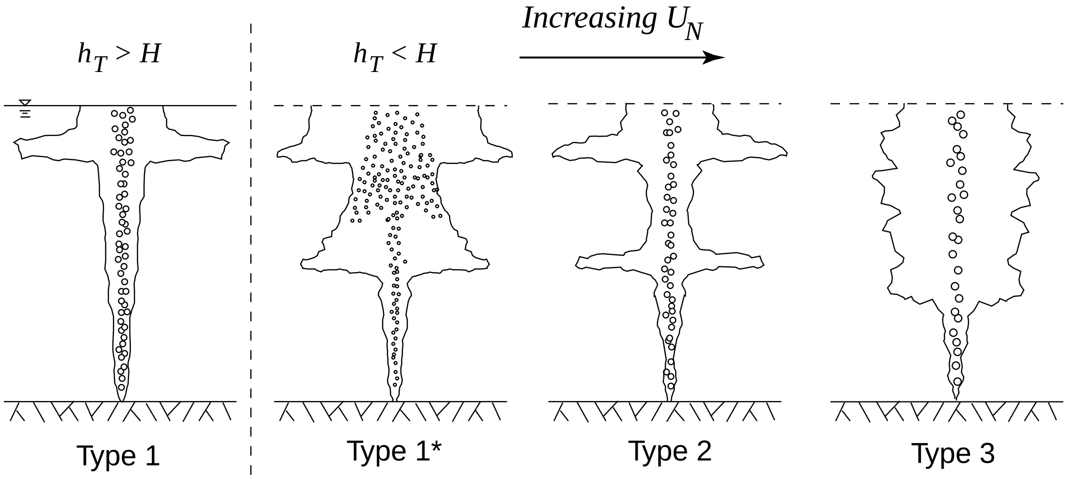

Figure 1-2: Two phase plume types. Source: (Socolofsky 2001)

peel with the fluid. Type 2 plumes, with U_N of about 1.5 to 2.4, exhibit multiple distinct peels. Type 3 plumes, for U_N greater than about 2.4, are characterized by continuous, overlapping peeling. Part of the challenge of modeling two phase plumes is describing this peeling behavior accurately.

1.3 Description of Numerical Model

1.3.1 Integral Models

Integral techniques simplify numerical modeling of unbounded flows. In an integral model, flow properties such as plume width and fluxes are assumed to be self-similar and a function of propagation direction only. With this assumption, and the use of the entrainment hypothesis, the problem is reduced from a 3-D boundary value problem to a 1-D initial value problem. Alternatively, 3-D modeling of two-phase plumes has been applied successfully to liquid CO_2 injections by Alendal & Drange (2001), Chen (2001), and Sato & Hama (2001). The main advantages of the integral technique are that it is computationally inexpensive in comparison to a numerical solution of the Navier-Stokes equations, and that it allows phys-

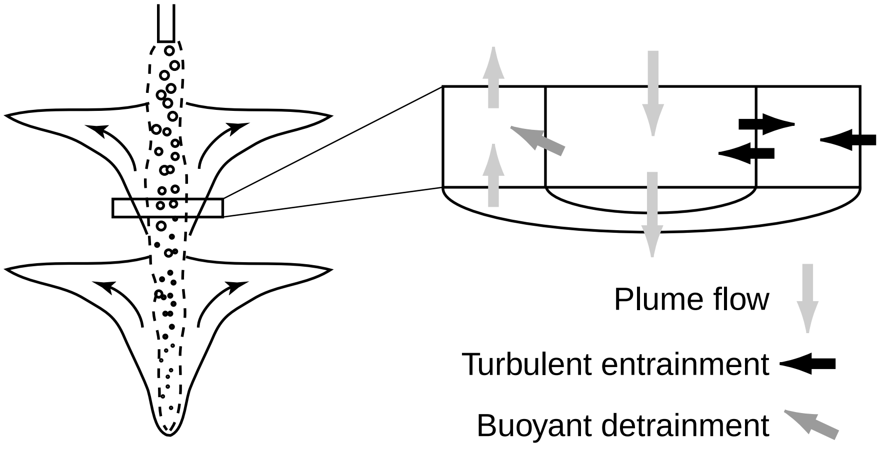

Figure 1-3: Integral Model Control Volume.

ical insight to be used explicitly in model formulation. However, two-phase plumes strain the self-similarity assumption and turbulence must be explicitly parameterized. Of course, the validity of any numerical model is subject to experimental verification.

1.3.2 Model Control Volume and Fluxes

A hybrid, double-plume integral model is used in this study. The model is that described by Crounse (2000), employing the counter flowing approach introduced by Asaeda & Imberger (1993) modified for liquid CO_2 injection. In this type of double plume model, the dispersed phase and associated entrained water are modeled as an inner plume, while the counter-flowing intrusions created from peeling events are modeled as an outer plume. Figure 1-3 shows a schematic of the model control volume.

The plume evolution is described by entrainment fluxes from the ambient to the outer plume, from the outer to the inner plume and vice versa, and detrainment from the inner plume through peeling as indicated in Figure 1-3. Following the entrainment assumption of Morton (1962) for coaxial jets, the entrainment fluxes are defined as

$$\begin{aligned} E_i &= 2\pi b_i \alpha_i (u_i - u_o) && (1.2) \\ E_o &= 2\pi b_i \alpha_o u_o && (1.3) \\ E_a &= 2\pi b_o \alpha_a u_o. && (1.4) \end{aligned}$$

where E_i, E_o, and E_a are the entrainment fluxes per unit height from the outer plume to the inner plume, from the inner to the outer plume, and from the ambient environment to the outer plume, respectively. u_i and u_o are the inner and outer plume velocities, b_i and b_o are the inner and outer plume widths, and α_i, α_o and α_a are entrainment coefficients governing the three entrainment fluxes. The entrainment coefficients are calibrated in Chapter 3.

A novel parameterization for the detrainment flux, or peeling, has been introduced in the current model. Crounse defines the peeling flux as

$$E_p = \epsilon \left(\frac{u_s}{u_i} \right)^2 \left(\frac{B_i}{u_i^2} \right) \qquad (1.5)$$

where B_i is the inner plume buoyancy flux and ϵ is an empirical parameter that is calibrated later in this work. Equation 1.5 is a new approach in that it models peeling as a continuous flux and thus can model Type 3 behavior and allow for fractional peeling dependent on local plume conditions. This differs from previous models by McDougall (1978), Asaeda & Imberger (1993), and Schladow (1992) that assume a constant fraction of plume water peels in each event and/or peeling occurs only in discrete events. With the model fluxes defined, the model equations can be developed.

1.3.3 Model Implementation

Integral equations based on conservation of mass, momentum, salt, heat and dispersed phase concentration for the inner, rising plume and the outer, falling plume provide a set of governing equations for the problem. A complete, detailed description may be found in Crounse (2000). A fourth-order adaptive step Runge-Kutta algorithm is used for the integration of the governing equations. After setting initial conditions, the model proceeds iteratively by integrating the inner plume downwards, then integrating the outer plume upwards until convergence is reached. A relaxation scheme is used due to the fluctuating nature of the problem. The model has been programmed in C++, and includes a TCL/Tk graphical user interface. The model is used essentially as described in Crounse (2000), except it has been turned upside-down, relevant phase properties related to CO_2 hydrates have been added, and the capability to model multiple particle sizes has been introduced.

1.4 Goals of this Work

The overarching goal of this study is to investigate the characteristics of the release of CO_2 hydrate particles in the deep ocean. Relevant properties and capabilities that have been added to the integral model are summarized in Chapter 2. Chapter 3 includes calibration work on plume heights and volume fluxes, buoyant detrainment (peeling), descending model functionality, and mass transfer. Chapter 4 presents the results of CO_2 hydrate particle plume modeling, including the effects of mass flux, particle radius, and particle size distribution on plume depth and CO_2 dilution. Chapter 5 provides some insight into alternate CO_2 hydrate release scenarios, and conclusions and recommendations for further work are contained in Chapter 6.

Chapter 2

Chemical and Physical Properties

2.1 CO_2 Hydrates

2.1.1 Formation

When pure CO_2 is introduced into water at the low temperatures and high pressures of the deep ocean, a clathrate hydrate tends to form. Figure 2-1 shows a phase diagram for the CO_2 / water system. Figure 2-2 shows the types of structures that natural gas hydrates may adopt. In these structures, water molecules form the outer "cage" with gas molecules occupying the cavities. Naturally occuring hydrates tend to form either Structure I or Structure II, with 2-16 gas molecules occupying the cavity formed by the water molecules (Sloan 1998). A molecule of CO_2 hydrate consists of approximately six water molecules surrounding one CO_2 molecule. In this work, the molecular weight used for CO_2 hydrates is 152 $g/mole$, consistent with the molecular formula $6H_2O \cdot CO_2$. Also, of particular interest to this study, the density of CO_2 hydrate is approximately 1.1 g/cm^3 (Aya et al. 1997), which is greater than that of seawater.

Previous work has focused on the mass transfer implications of the formation of a hydrate film on the edge of CO_2 droplets, e.g. (Fujioka et al. 1994, Hirai et al. 1997, Mori & Mochizuki 1998). Research is now proceeding to investigate the possibility of creating solid CO_2 hydrate particles, which is the main motivation for this work. ORNL has succeeded in creating an extruded, solid hydrate coil in labratory settings. It is conceivable that nozzle designs could

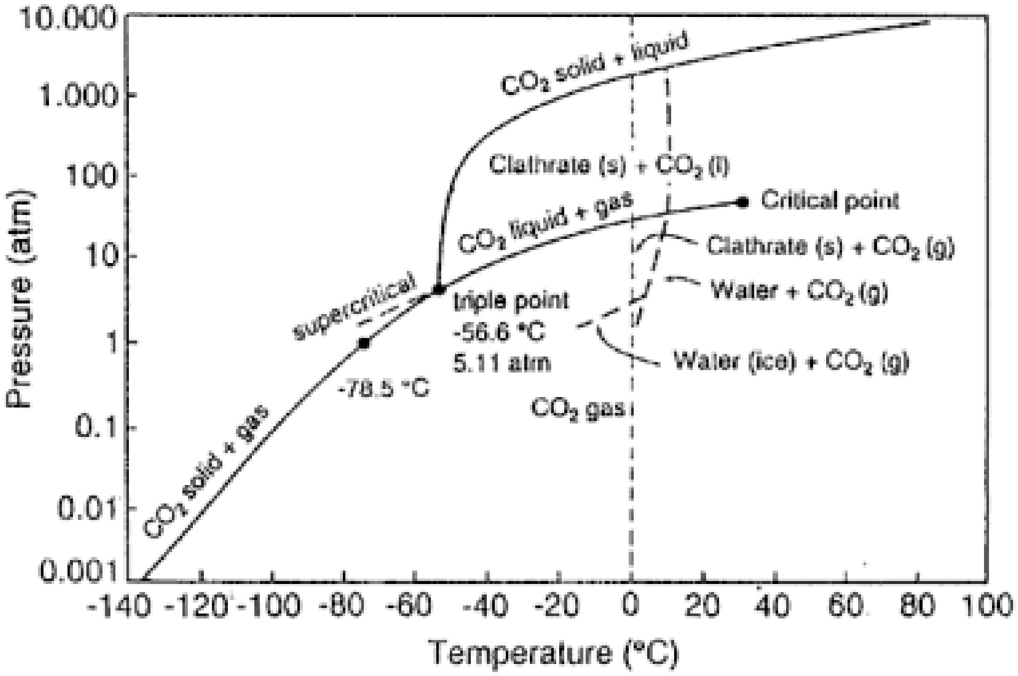

Figure 2-1: Phase Diagram for CO_2 in the presence of water. Source: Murray et al. (1996)

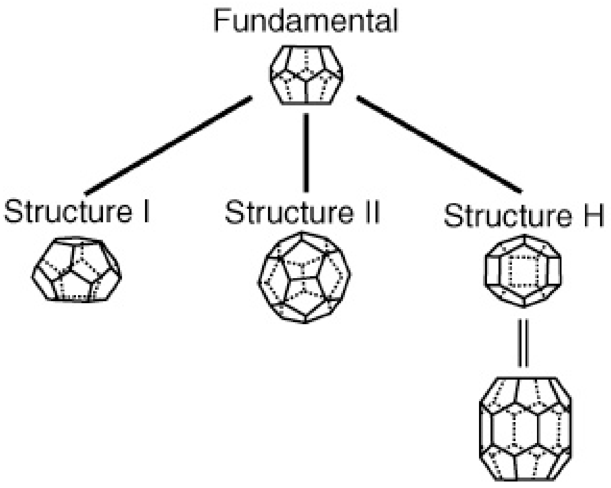

Figure 2-2: Typical gas clathrate hydrate structures. Source: Sloan (1998)

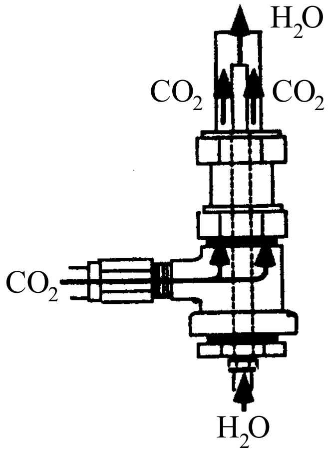

Figure 2-3: CO_2 hydrate forming nozzle. Source: Hirai et al. (1999)

be created to create hydrate particles *in-situ*. In fact, this has been partially done. Hirai et al. (1999) introduced a nozzle design whereby water introduced into pure CO_2 in the nozzle assembly before ocean release creates hydrate particles within CO_2 droplets (Figure 2-3). Holder et al. (2001) demonstrates the formation of CO_2 hydrates from a CO_2 rich water solution. Rehder et al. (2001) created a solid plug of CO_2 hydrate for ocean floor dissolution experiments. With a tentative idea of how these hydrates might be formed, some of their properties are postulated.

2.1.2 Mass Transfer

Before describing the mass transfer model used in this study, it is helpful to take a heuristic look at the differences between liquid CO_2 and CO_2 hydrates in terms of mass transfer behavior. For liquid CO_2 droplets, the rate of mass transfer is expected to be proportional to a surface area, mass transfer coefficient, and surface concentration of CO_2:

$$\frac{dM_c}{dt} = -AKC_s \tag{2.1}$$

where A is the droplet surface area, K is a mass transfer coefficient which depends on particle size and velocity, and C_s is the surface concentration which is identical to the solubility of

CO_2 in the ambient.

Crounse (2000) extended this model to apply to hydrate-coated CO_2 droplets by introducing an inhibition factor, λ, to match experimental observations (e.g. (Hirai et al. 1997)) without delving over much into the details of hydrate chemistry. This factor is expected to account for uncertainties in C_s caused by the presence of a hydrate shell. The new proportionality is thus

$$\frac{dM_c}{dt} = -\lambda AKC_s. \tag{2.2}$$

In the current work this mass transfer model is further extended to apply to solid CO_2 hydrate particles. The mass transfer rate of CO_2 hydrates, composed of about 70% water, is still expected to depend on the surface concentration of CO_2. However, the mass transfer expression must be modified by the factor MW_{hyd}/MW_{CO_2} to account for the fact that every molecule of dissolving CO_2 yields the loss of its associated water molecules as well. λ remain in Equation 2.3 as the surface concentration and validity of this model are somewhat uncertain (for instance, it is possible that a heat transfer limited model would be more appropriate).

$$\frac{dM_h}{dt} = -\lambda AKC_s\frac{MW_{hyd}}{MW_{CO_2}}. \tag{2.3}$$

For now, the validity of this expression will be verified through comparison to the sparse experimental data that is available.

Following the above logic, the mass transfer model presented in Crounse (2000) has been modified slightly for hydrate particle dissolution. Furthermore, the capability to model a distribution of particle sizes has been added. The rate of dissolution for each particle size is described by the empirical Ranz-Marshall equation:

$$\frac{dm_{p,j}}{dt} = -\pi\lambda d_{p,j}^2 K_j(C_s - c)\frac{MW_{hyd}}{MW_{CO_2}} \tag{2.4}$$

where $m_{p,j}[M]$ is the mass contained in particle of diameter $d_{p,j}[L]$, λ is an empirical coefficient added to account for hydrate induced mass transfer inhibition, $K_j[L/T]$ is a mass transfer coefficient corresponding to the jth particle diameter, $C_s[M/L^3]$ is the surface concentration or solubility of CO_2, $c[M/L^3]$ is the concentration of dissolved CO_2 in the vicinity of the particle, and MW_{hyd}/MW_{CO_2} is the ratio of molecular weights. Transforming Equation 2.4 as in Crounse (2000) by substituting $m_p = \frac{1}{6}\pi d_{p,j}^3 \rho_p$, then defining $\Lambda = \lambda MW_{hyd}/MW_{CO_2}$ for convenience, yields the diameter shrinkage rate for particle size j:

$$\frac{dd_{p,j}}{dt} = -2\Lambda K_j \frac{(C_s - c)}{\rho_p} \tag{2.5}$$

Multiplying Equation 2.5 by the bubble number flux in size fraction j describes the jth rate of change in the mass flux of CO_2 in the dispersed phase. Furthermore, by dividing by the nominal bubble velocity, $(u_i + u_{p,j})$ ($u_{p,j}$ is the slip velocity for particle j), the equation describes a change over distance rather than time in accordance with the plume model governing equations.

$$\frac{dW_{p,j}}{dz} = -N_{p,j}\pi\Lambda d_{p,j}^2 \frac{K_j(C_s - c)}{(u_i + u_{p,j})} \tag{2.6}$$

Finally, by summing Equation 2.6 over all of the particle sizes, the total change in dispersed phase mass is found:

$$\frac{dW_p}{dz} = \sum_{j=1}^{n} -N_{p,j}\pi\Lambda d_{p,j}^2 \frac{K_j(C_s - c)}{(u_i + u_{p,j})} \tag{2.7}$$

Since this is a flux of CO_2 hydrate, the flux of pure CO_2 from the dispersed phase can be calculated by multiplying Equation 2.7 by the ratio of molecular weights, MW_{CO_2}/MW_{hyd}.

The mass transfer coefficient remains to be determined. Crounse (2000) found acceptable results for the mass transfer rate from a hydrate-coated CO_2 droplet by using a mass transfer coefficient correlation from Clift et al. (1978), with $\lambda = 0.5$. The mechanism for the dissolution of a hydrate-coated CO_2 droplet has been postulated as dominated by the diffusion of CO_2 molecules through the hydrate shell (Radhakrishan et al. 2001). It is unclear whether the behavior of a solid hydrate particle would be similar. However, preliminary data from Rehder et al. (2001) indicate that the diameter shrinkage rate of hydrate particles is quite similar to that of liquid CO_2 droplets with a hydrate shell. This indicates that the value of λ should be lower for solid hydrates than for hydrate covered liquid droplets, as the ratio MW_{hyd}/MW_{CO_2} acts to increase the shrinkage rate.

For the purposes of the current study, a mass transfer coefficient as described in Crounse will be used, along with a λ determined by comparison with experimental data. Crounse (2000) shows that model predicted plume structure (e.g. peel height) is quite sensitive to mass transfer; however, CO_2 concentration is not. It is important to consider the uncertainty in mass transfer while evaluating any model results.

2.1.3 Particle Size Distribution

As described above, the ability to model a host of particle sizes at one time has been added to the model. Although the model is programmed to handle only discrete fractions of different sizes, it is possible to approximate the shape of continuous distributions. The method of formation of CO_2 hydrate particles is uncertain, and hence, so is the distribution of particle sizes. For the purposes of determining model sensitivy to particle distribution, some plausible distributions and extreme cases are explored.

The expected effect of a distribution of particles arises from the dependence of mass transfer rate and slip velocity on particle size. In general, larger particles will have a slower dissolution rate over distance due to their lower surface area to volume ratio and higher slip velocity. This is shown in Figure 2-4, where modeled diameter versus depth is plotted for three isolated, falling hydrate particles of varying initial diameters. The large particles descend markedly further than the small ones.

Figure 2-5 shows some possible particle distributions, each with a mean of 0.5 cm and a standard deviation of 0.15 cm. An equal amount of mass distributed in each of a few different sizes yields the uniform distribution, which would conceivably distribute mass more evenly over plume depth, with small particles dissolving rapidly near the release and larger particles dissolving at greater depths. The normal distribution represents a more likely distribution of mass than the uniform, and should behave somewhere in between the monodisperse and uniform cases. Finally, the log-normal distribution is frequently used to represent the size distibrution of sediment particles (Crowe et al. 1998). Because of the skewed nature of the log-normal distribution, it is hypothesized to cause a high amount of dissolution near the release, with the "tail" of larger particles reaching greater depths. Chapter 4 examines the magnitude of particle distribution effects.

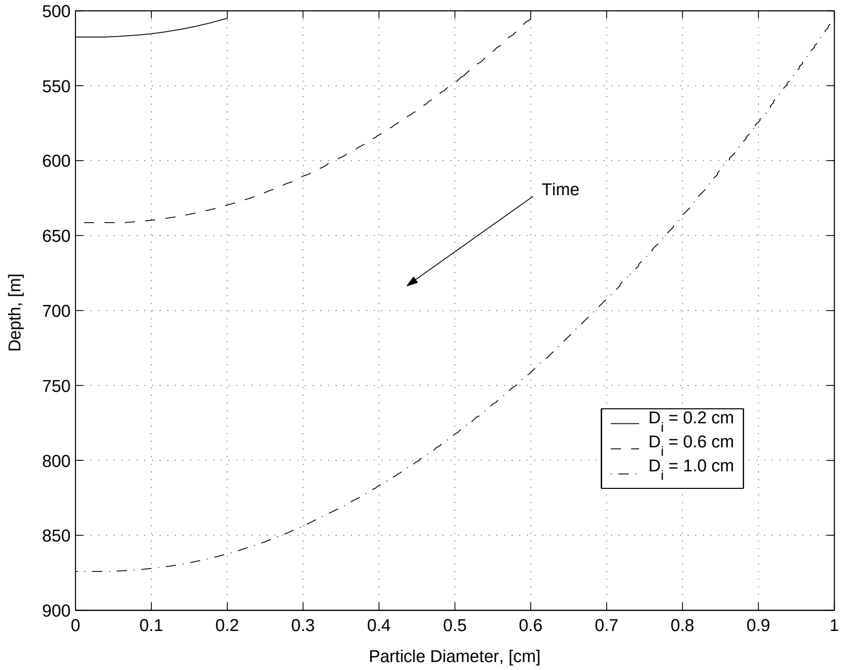

Figure 2-4: Falling, isolated particle diameter vs. depth for hydrate particles of different initial diameters released at 500m depth.

2.1.4 Particle Slip Velocity

Depending on the method of CO_2 hydrate formation, the particles may assume different shapes and sizes. Formation techniques similar to the formation of hydrate particles within CO_2 droplets (Hirai et al. 1999) could create spheres, while ORNL techniques might create cylinders or coils. In the absence of a definitive particle shape, a spherical geometry will be assumed, with the slip velocity correlation detailed in Crounse (2000).

2.2 Carbonate Chemistry

2.2.1 CO_2 in water

One of the main environmental concerns of ocean sequestration is the fact that CO_2 is a weak acid in water. Hence, the addition of large amounts of CO_2 into the ocean will tend to lower the ambient pH, and potentially impact marine biota. Dissolved CO_2 in water is

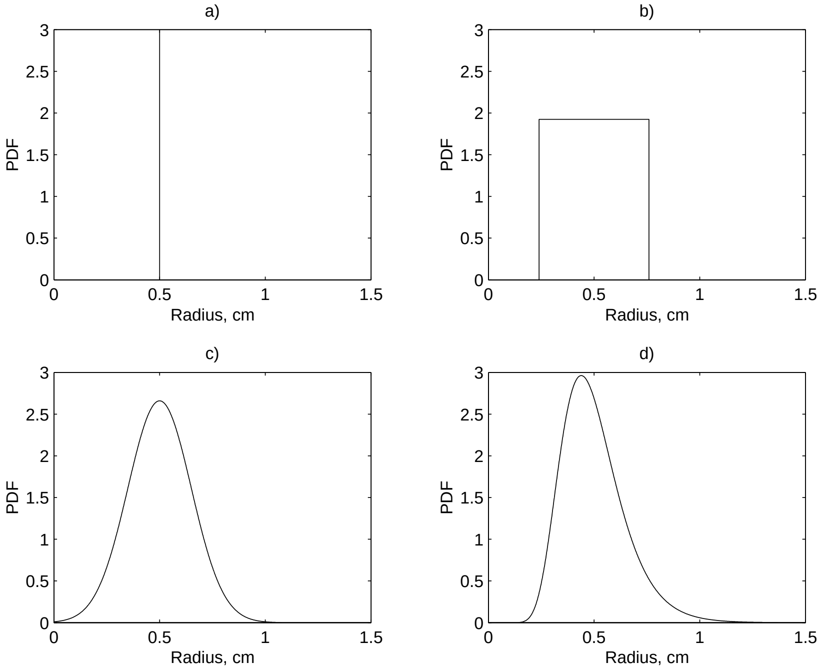

Figure 2-5: Example particle size distributions with mean = 0.5 cm. a) Monodispersed, b) Uniform distribution, c) Gaussian distribution, d) Log-normal distribution.

a part of the carbonate system, composed of the carbonate ion (CO_3^{2-}), the bicarbonate ion (HCO_3^-), and carbonic acid (H_2CO_3). Because of its importance in the chemistry of natural waters, the chemistry of the carbonate system has been studied in detail. The major chemical reactions are (Morel & Hering 1993):

$$\begin{aligned} H_2O &\rightleftharpoons H^+ + OH^- && (2.8) \\ CO_2(aq) + H_2O &\rightleftharpoons H_2CO_3 && (2.9) \\ CO_2(aq) + H_2O &\rightleftharpoons HCO_3^- + H^+ && (2.10) \\ H_2CO_3 &\rightleftharpoons HCO_3^- + H^+ && (2.11) \\ HCO_3^- &\rightleftharpoons CO_3^{2-} + H^+. && (2.12) \end{aligned}$$

Typically, dissolved CO_2 and H_2CO_3 are summed and denoted $H_2CO_3^*$, allowing equations 2.9-2.11 to be replaced with:

$$H_2CO_3^* \rightleftharpoons HCO_3^- + H^+. \qquad (2.13)$$

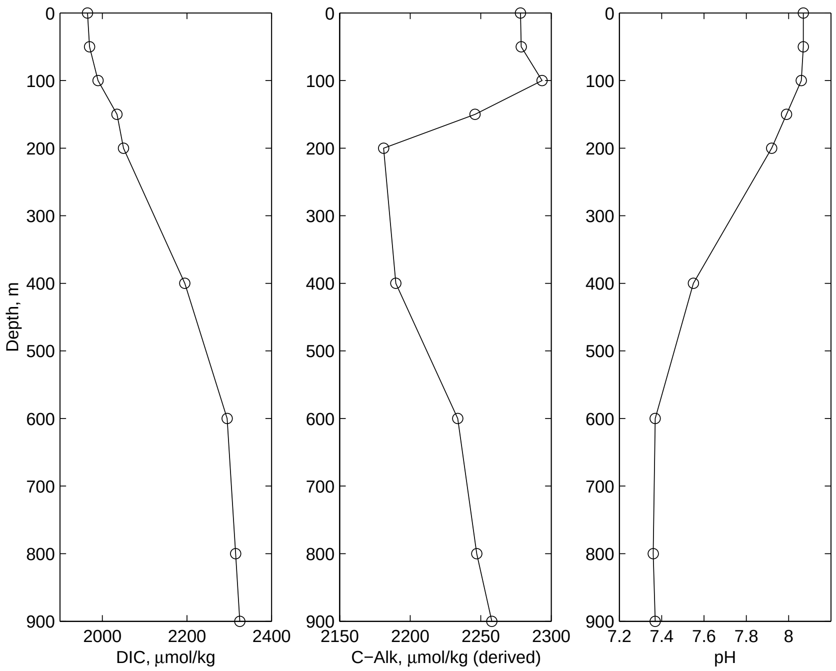

Figure 2-6: Profiles of DIC, $C - alk$, and pH from near Keahole Point, Hawaii. $C - alk$ is calculated from pH and DIC as described below (Miller et al. 2000).

The equilibrium constants of these reactions are known quite well as a function of temperature and salinity (Dickson & Goyet 1994, Roy et al. 1993). For equilibrium calculations it is helpful to define the carbon alkalinity, $C - Alk$ and the dissolved inorganic carbon (DIC) (Morel & Hering 1993):

$$
\begin{aligned}
C - Alk &= -[H^+] + [OH^-] + [HCO_3^-] + 2[CO_3^{2-}] && (2.14) \\
DIC &= [H_2CO_3^*] + [HCO_3^-] + [CO_3^{2-}]. && (2.15)
\end{aligned}
$$

DIC is simply a sum of the inorganic carbonate species, while $C - Alk$ is, in one sense, an indicator of a water's weak acid buffering capacity. In natural waters, $C - Alk$ is typically the major component of total alkalinity. Note that $C - Alk$ does not change with added CO_2. Profiles of $C - Alk$, DIC, and pH from near Keahole Point, Hawaii are shown in Figure 2-6.

The magnitude of ambient DIC concentration has some implications for mass transfer.

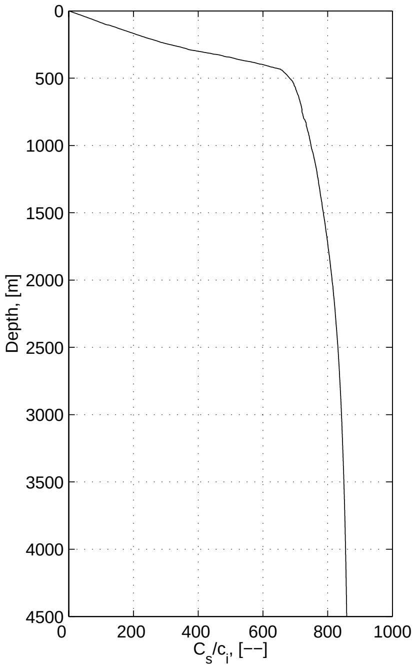

Figure 2-7: Comparison of CO_2 solubility, C_s, and maximum ambient CO_2 concentration, c_i. c_i is approximated conservatively as DIC.

If DIC is sufficiently large, mass transfer may be inhibited by reducing the driving force $(C_s - c_i)$. Note that c_i, the concentration of dissolved CO_2, is only a fraction of DIC at typical ocean water pH. Figure 2-7 shows the ratio C_s/c_i vs. depth, where C_s is the model predicted CO_2 solubility and c_i is taken as an average DIC concentration of 2300 $\mu mol/kg$ for simplicity. In the depth range of interest, below 500m, C_s is hundreds of times greater than the maximum possible ambient dissolved CO_2 concentration. Hence, the ambient DIC profile has a negligible effect on mass transfer and is in fact ignored in the model.

2.2.2 pH calculations

$C - Alk$, DIC, and pH form a convenient set of parameters in that if any two of them are known, the other can be calculated. In the case of a CO_2 hydrate release, $C - Alk$ and DIC are known reasonably well, and therefore the pH may be calculated. In this work, pH calculations are limited to plume intrusions and intermediate field dilution estimates, and hence are unaffected by the kinetic effects mentioned by Zeebe et al. (1999).

Morel & Hering (1993) detail a method for solving for pH given any combination of $C - Alk$ and DIC. A brief summary of this method follows, with the addition that it has been generalized to include acidity constants based on the total hydrogen ion concentration, and given as a function of temperature and salinity by Dickson & Goyet (1994) and Roy et al. (1993).

First, mass laws for the dissociation of water, carbonic acid, and bicarbonate are defined (from reactions 2.8, 2.13, and 2.12):

$$
\begin{aligned}
[OH^-] &= 10^{-pK_w}[H^+]^{-1} && (2.16)\\
[HCO_3^-] &= 10^{-pK_1}[H^+]^{-1}[H_2CO_3^*] && (2.17)\\
[CO_3^{2-}] &= 10^{-(pK_1+pK_2)}[H^+]^{-2}[H_2CO_3^*] && (2.18)
\end{aligned}
$$

where pK_w, pK_1, and pK_2 are the dissociation constants for water, carbonic acid, and bicarbonate. The dissociation constants are calulated according to Dickson & Goyet (1994):

$$
\begin{aligned}
pK_w &= -1/\ln 10 \Big[\frac{-13847.26}{T} + 148.9652 - 23.6521 \ln T + \\
&\quad \left(\frac{118.97}{T} - 5.977 + 1.0495 lnT\right) S^{1/2} - 0.01615S\Big] && (2.19)\\
pK_1 &= -1/\ln 10 \Big[\frac{-2307.1266}{T} + 2.83655 - 1.5529413 \ln T + \\
&\quad \left(\frac{-4.0484}{T} - 0.20760841\right) S^{1/2} + 0.08468345S \\
&\quad - 0.00654208S^{3/2} + \ln(1 - 0.001005S)\Big] && (2.20)\\
pK_2 &= -1/\ln 10 \Big[\frac{-3351.6106}{T} - 9.226508 - 0.2005743 \ln T + \\
&\quad \left(\frac{-23.9722}{T} - 0.106901773\right) S^{1/2} + 0.1130822S \\
&\quad - 0.00846934S^{3/2} + \ln(1 - 0.001005S)\Big] && (2.21)
\end{aligned}
$$

where T is temperature in Kelvins and S is salinity in psu. Equations 2.16 to 2.18 may be inserted into the expression for DIC (Equation 2.15) to yield expressions for the carbonate species concentrations:

$$\begin{aligned}
[H_2CO_3^*] &= \alpha_0 DIC && (2.22)\\
[HCO_3^-] &= \alpha_1 DIC && (2.23)\\
[CO_3^{2-}] &= \alpha_2 DIC && (2.24)
\end{aligned}$$

where the $\alpha's$ are the ionization fractions defined as:

$$\begin{aligned}
\alpha_0 &= (1 + 10^{-pK_1}[H^+]^{-1} + 10^{-(pK_1+pK_2)}[H^+]^{-2})^{-1} && (2.25)\\
\alpha_1 &= (1 + 10^{pK_1}[H^+] + 10^{-pK_2}[H^+]^{-1})^{-1} && (2.26)\\
\alpha_2 &= (1 + 10^{pK_2}[H^+] + 10^{(pK_1+pK_2)}[H^+]^2)^{-1}. && (2.27)
\end{aligned}$$

Finally, Equations 2.8 and 2.22 through 2.24 may be substituted into Equation 2.14:

$$C - Alk = -[H^+] + 10^{-pK_w} + \alpha_1 DIC + 2\alpha_2 DIC \qquad (2.28)$$

Equation 2.28 is an implicit function of $[H^+]$. It is therefore necessary to use a zero finding algorithm to find $[H^+]$ given $C - Alk$ and DIC. Since the dissociation constants are calibrated to give the total hydrogen ion concentration, $[H^+]$, and pH meters typically measure the free hydrogen concentration, $\{H^+\}$, it is helpful to calculate free hydrogen from the above result.

Dickson & Goyet (1994) defines the total hydrogen ion concentration as

$$[H^+] = \{H^+\}(1 + S_T/K_S) \qquad (2.29)$$

where S_T is the total sulfate concentration ($[HSO_4^-] + [SO_4^{2-}]$), and K_S is the dissociation constant for HSO_4^-. K_s is calculated as:

$$\begin{aligned}
pK_S &= -1/\ln 10 \Big[\frac{-4276.1}{T} + 141.328 - 23.093 \ln T + \\
&\quad \Big(\frac{-13856}{T} + 324.57 - 47.986 \ln T\Big) I^{1/2} +
\end{aligned}$$

$$\left(\frac{35474}{T} - 771.54 + 114.723\ln T\right) I$$
$$\left.\frac{2698}{T}I^{3/2} + \frac{1776}{T}I^2 + \ln(1 - 0.001005S)\right] \qquad (2.30)$$

where

$$I = \frac{19.924S}{1000 - 1.005S}. \qquad (2.31)$$

By assuming a total sulfate concentration typical of seawater, $S_T = 0.0284 \cdot molkg - soln^{-1}$ at a salinity of 35 psu, $\{H^+\}$ may be approximated.

2.3 Seawater

Ambient profiles of density and pressure are needed to determine plume and dispersed phase buoyancy. A profile of temperature and salinity collected at Station Aloha, north of Oahu, is used because it extends to 4500 m depth. From this profile, ambient density may be calculated, including the solute density effect due to CO_2 dissolution as detailed in Crounse (2000). It should be noted that the release of heat due to CO_2 hydrate dissociation and CO_2 dissolution, equal to 73 and 25 kJ/mol (Sloan 1997, Crounse 2000), respectively, slightly counteract the solute density effect as density is a decreasing function of temperature. Figure 2-8 shows density as a function of depth for CO_2 hydrates (assumed incompressible), seawater (both with and without compression), and seawater with the maximum possible CO_2 solute density effect. The maximum possible solute density effect is taken as that at CO_2 saturation. Although it is not expected that plume water would reach CO_2 saturation, it is apparent that the density effect could be significant.

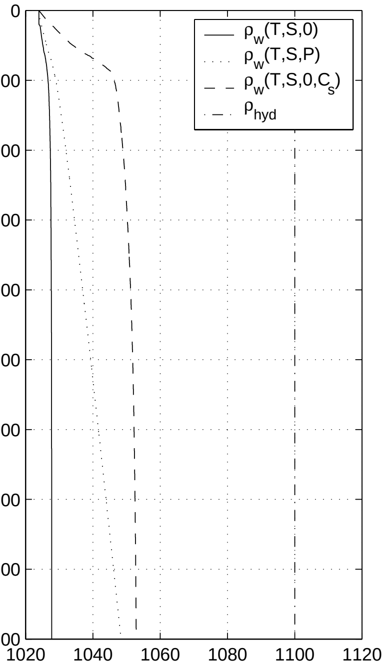

Figure 2-8: Ambient density profile including seawater density at atmospheric and $in-situ$ pressure, CO_2 hydrate density, and the maximum density of seawater at atmospheric pressure including the solute density effect of saturated CO_2 concentration

Chapter 3

Model Validation

The validity of any theoretical model is subject to verification from experimental data. As far as the author knows, there is no experimental data available for a descending two-phase plume where dissolution of the dispersed phase acts to increase plume water density. However, in the absence of such data, certain aspects of the model can be verified against data that is available. Validation begins with a verification of first peel properties including trap height, volume fluxes, and buoyant detrainment, continues with a basic check of the model functionality, and concludes with an investigation of the mass transfer model.

3.1 Trap Height and Volume Fluxes

Experimental data on the trap height and volume fluxes of the first peeling event provide a means for calibrating the entrainment coefficients associated with Equations 1.2-1.4. Crounse (2000) compared model accuracy for different sets of entrainment coefficients, yielding no clear optimum set. With the benefit of additional experimental data from Socolofsky (2001), two of Crounse's sets are examined for the current study. Set A, favored by Asaeda & Imberger (1993) and McDougall (1978), consists of $\alpha_i = 0.055$, $\alpha_o = \alpha_a = 0.11$. Set B, given by Crounse as the best fit for volume flux data, consists of $\alpha_i = 0.04$, $\alpha_o = 0.11$ and $\alpha_a = 0.06$. The model output produced by these coefficients is compared against data for two values of the peeling parameter, ϵ, which appears in Equation 1.5.

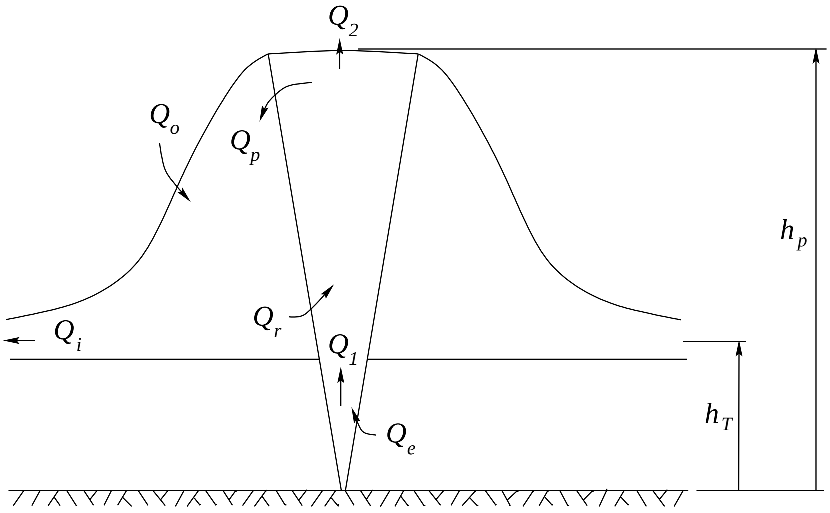

Figure 3-1: Schematic of plume fluxes. Source: Socolofsky (2001).

Figure 3-1 shows the conceptual model used by Socolofsky for the analysis of multi-phase plume experiments. We will calibrate against experimental values for Q_1, Q_2, Q_p, Q_o, Q_i, h_p , and h_T. Of particular import for ocean sequestration are Q_i and h_T, as the former helps determine DIC upon intrusion into the ambient and the latter determines sequestration depth.

3.1.1 Trap Height

Trap height data were available from Socolofsky (2001) and Reingold (1994); Socolofsky (2001) also presented peel height data. These data include both air (ascending) and sediment (descending) plume data. Data have been chosen within the range of model applicability of $U_N = 1.5 - 3.5$. Table 3.1 shows experimental trap and peel height data, model predicted heights, and percent error magnitude for $\epsilon = 0.005$. A value of $\epsilon = 0.005$ is found to match buoyant detrainment data in Section 3.2. All heights have been non-dimensionalized by the characteristic plume height, $(B/N^3)^{1/4}$.

Set A and Set B give similar predictions for plume heights, with Set A performing slightly better for trap height and Set B giving the lower overall average error. Figure 3-2 shows model output using Set A and Set B with different ϵ values, plotted alongside experimental data and empirical correlations from Socolofsky (2001). Both Set A and Set B match favorably

	U_N	Measured Height	Model Height, Set A	Set A % error	Model Height, Set B	Set B % error
$\frac{h_T}{(B/N^3)^{1/4}}$	1.66	2.59	2.27	12	2.65	2
	1.68	3.17	2.30	28	2.73	14
	2.24	2.99	2.14	28	2.53	15
	2.25	2.01	2.18	8	2.60	29
	2.91	2.86	1.74	39	2.09	27
	2.97	1.68	1.90	13	2.36	40
$\frac{h_p}{(B/N^3)^{1/4}}$	1.66	4.48	3.60	20	4.48	0
	1.68	6.02	3.66	39	4.59	24
	2.24	5.39	3.51	35	4.29	20
	2.91	4.64	2.90	38	3.6	23
Average Error,%		–	–	26	–	19
Average h_T Error,%		–	–	21	–	21

Table 3.1: Trap and Peel height data for $\epsilon = 0.005$.

with Socolofsky's correlation for trap height, and under predict the peel height correlation. Since trap height is the more important parameter for the predictions in this study, this is deemed acceptable. Predicted heights are fairly insensitive to changes in ϵ. Overall, the model does a reasonable job predicting plume heights given the spread of the available data.

3.1.2 Volume Fluxes

Volume flux data from the first peeling event, calculated in accordance with the conceptual model in Figure 3-1, were available from Socolofsky (2001). As with the trap height data, both ascending and descending plumes are included in the data, and only data in the range $U_N = 1.5 - 3.5$ were selected. The characteristic plume flux, $Q_c = (B^3/N^5)^{1/4}$ is used to non-dimensionalize all volume fluxes.

Experimentally determined volume flux data, model output for coefficient sets A and B, and percent error for $\epsilon = 0.005$ are listed Table 3.2. Set B produces noticeably lower total error (the average of all percent error magnitudes) and significantly lower Q_i (the average of all Q_1 percent error magnitudes) error than Set A. Figures 3-3 and 3-4 show the model

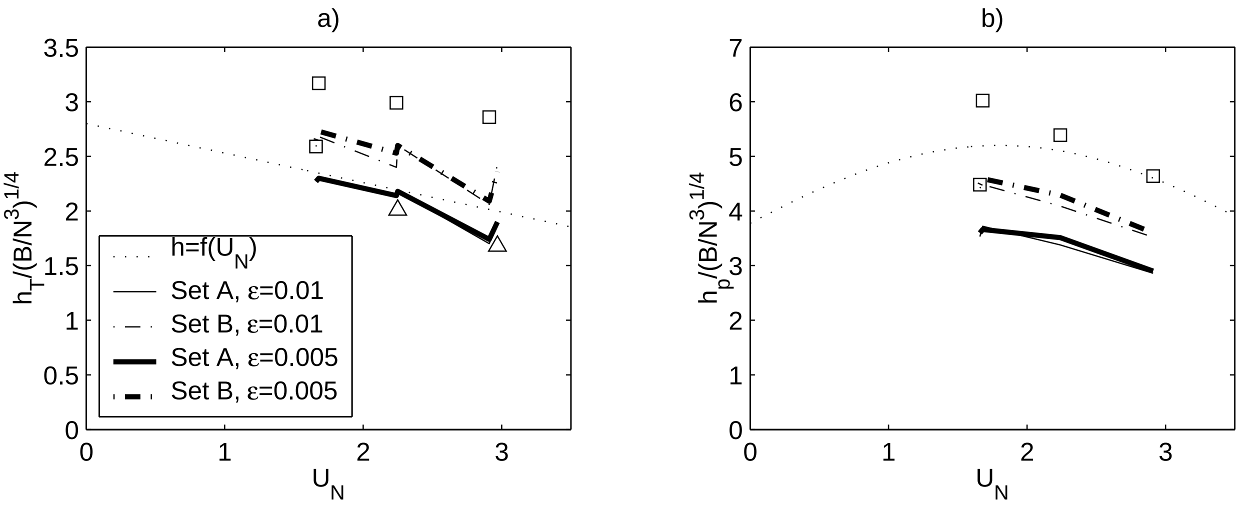

Figure 3-2: Comparison of modeled a) trap and b) peel heights with experimental data. Squares are data from Socolofsky (2001), triangles are data from Reingold (1994). Dotted lines are empirical fits from Socolofsky (2001).

output plotted alongside experimental data and empirical fits. Q_1 is better predicted by Set B, with best agreement at low U_N. Q_2 is predicted equally as well by both coefficient sets, and is in general under-predicted by a factor of two or three. Q_p is better predicted by Set A, although both sets underestimate this flux. Q_o and Q_i are both predicted very well by Set B at low U_N. This is important in that these fluxes are instrumental in determining CO_2 concentrations of plume water entering the ambient. Similar to the heights, the modeled fluxes are fairly insensitive to ϵ.

Overall, Sets A and B give almost equivalent prediction of heights associated with the first peel, while Set B gives the best prediction of volume fluxes. Set B predicts intrusion fluxes particularly well. Asaeda & Imberger (1993) used measures of plume height only to verify coefficient Set A, which agrees with the plume height data presented here. However, the larger sensitivity of plume volume fluxes to the entrainment coefficients points to the use of Set B presented above. It follows that entrainment coefficient Set B will be used for the model runs in this study.

	U_N	Measured Flux	Model Flux, Set A	Set A % error	Model Flux, Set B	Set B % error
$\frac{Q_1}{(B^3/N^5)^{1/4}}$	1.66	0.27	0.30	13	0.23	17
	1.68	0.23	0.29	27	0.22	3
	2.24	0.20	0.29	43	0.21	6
	2.91	0.17	0.16	7	0.12	29
$\frac{Q_2}{(B^3/N^5)^{1/4}}$	1.66	0.05	0.01	83	0.01	82
	1.68	0.03	0.01	70	0.01	75
	2.24	0.04	0.01	76	0.01	78
	2.91	0.05	0.01	83	0.01	86
$\frac{Q_p}{(B^3/N^5)^{1/4}}$	1.66	0.47	0.37	21	0.25	46
	1.68	0.63	0.37	42	0.26	59
	2.24	0.57	0.36	37	0.24	58
	2.91	0.44	0.18	60	0.12	72
$\frac{Q_o}{(B^3/N^5)^{1/4}}$	1.66	0.20	0.40	101	0.24	22
	1.68	0.28	0.37	32	0.24	14
	2.24	0.24	0.35	47	0.23	2
	2.91	0.26	0.15	41	0.11	60
$\frac{Q_i}{(B^3/N^5)^{1/4}}$	1.66	0.42	0.65	55	0.40	4
	1.68	0.49	0.66	34	0.45	7
	2.24	0.40	0.63	57	0.43	8
	2.91	0.37	0.30	19	0.21	44
Average Error,%		–	–	47	–	39
Average Q_i Error,%		–	–	41	–	16

Table 3.2: Volume flux data for $\epsilon = 0.005$.

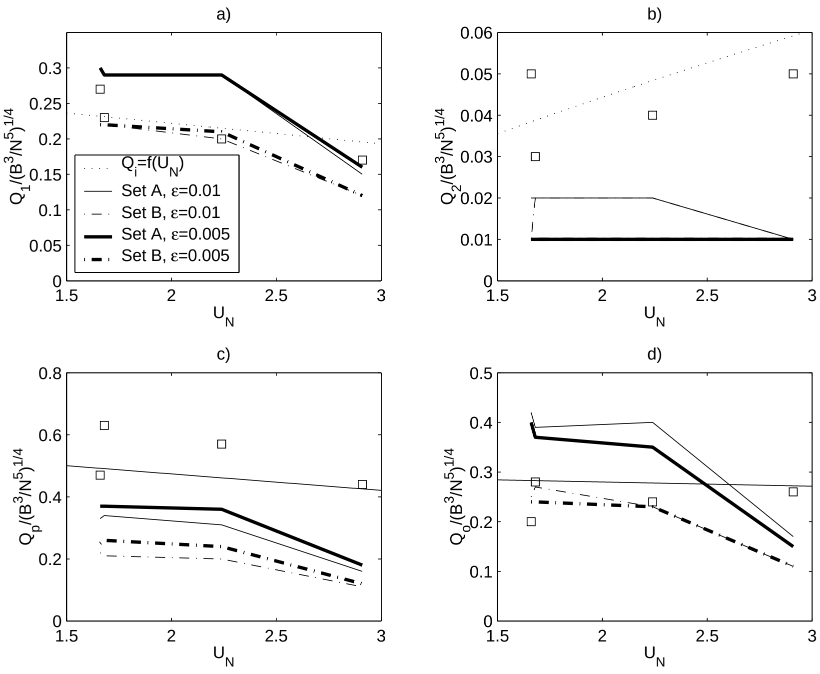

Figure 3-3: Comparison of modeled first peel volume fluxes with experimental data. a) Q_1, b) Q_2, c) Q_p, d) Q_o. Squares are data from Socolofsky (2001). Dotted lines are empirical fits from Socolofsky (2001).

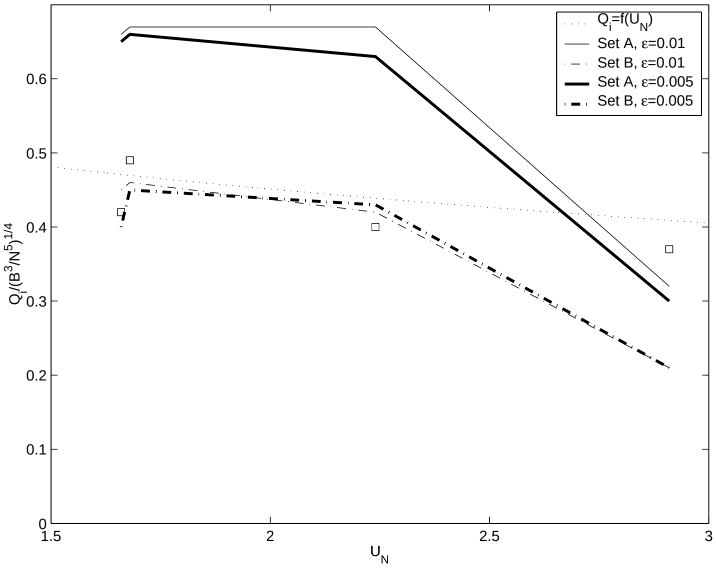

Figure 3-4: Comparison of modeled first peel intrusion flux with experimental data. Squares are data from Socolofsky (2001). Dotted lines are empirical fits from Socolofsky (2001).

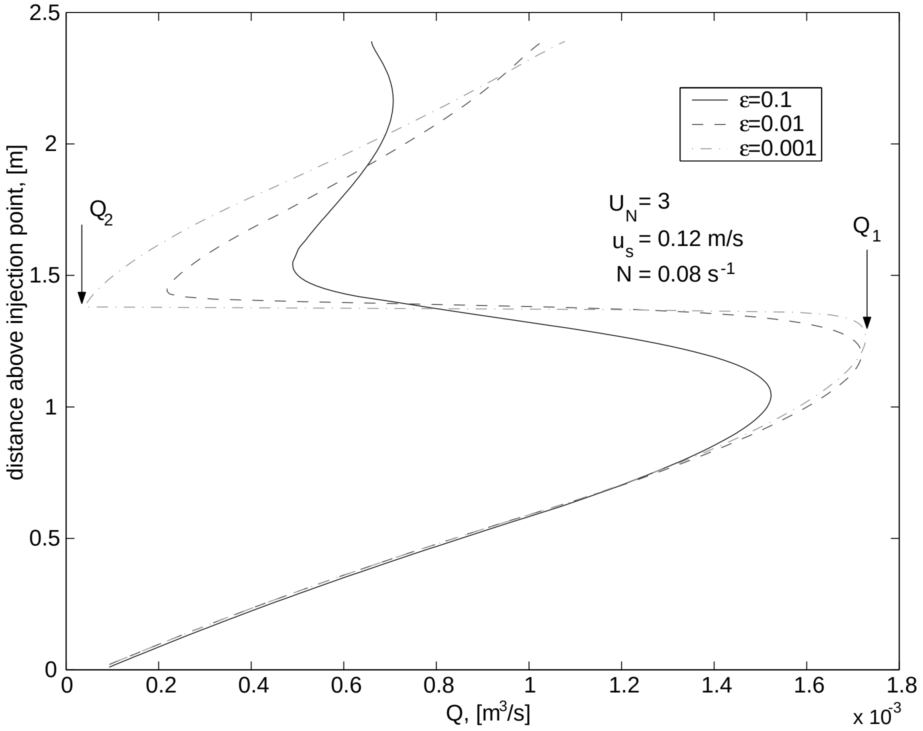

Figure 3-5: Definition of fluxes for peeling flux, f, calculation.

3.2 Buoyant Detrainment

Buoyant detrainment, or peeling, is calibrated via the peeling parameter, ϵ, from Equation 1.5. Socolofsky (2001) determined the fraction of plume water, f, that detrained from a two-phase plume in the first peeling event as a function of U_N (refer to Figure 3-8).

To effect a comparison with Socolofsky's data, the current model was used to predict plume behavior for a given U_N and ϵ. From the model output, the fraction of plume water that detrained in the first peeling event was calculated as

$$f = \frac{Q_1 - Q_2}{Q_2} \tag{3.1}$$

where Q_1 is the inner plume volume flux just before the onset of the first peel, and Q_2 is the inner plume volume flux after completion of the first peeling event. Figure 3-5 shows these fluxes schematically on representative model output for three values of ϵ. As indicated qualitatively on Figure 3-5, f is a decreasing function of epsilon. This dependence is indicated

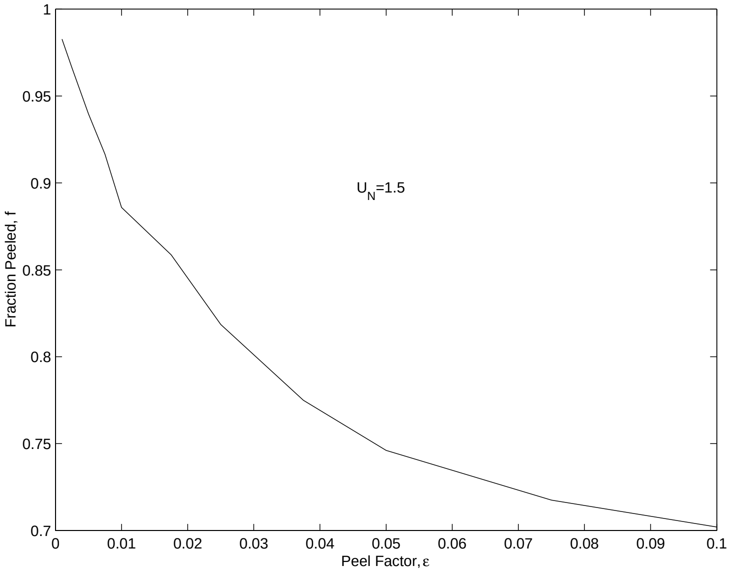

Figure 3-6: Model predicted f vs. ϵ for $U_N = 1.5$.

more concretely in Figure 3-6, where f vs. ϵ is plotted for $U_N = 1.5$. It follows that f can be varied rather significantly by varying ϵ, which is the basis of the calibration. Plotting f vs. ϵ for a few U_N yields the lines shown in Figure 3-7. Superimposed on these lines are points from Socolofsky (2001)'s fit to experimental f vs. U_N data. Projecting the experimental error from Socolofsky's points onto the f vs. ϵ curves indicates an acceptable range of ϵ for each U_N. The three values of U_N in Figure 3-7 show that there may be a slight dependence of ϵ on U_N, and that a reasonable value of ϵ lies in the range of 0.004-0.01. Model predicted f vs. U_N curves for several ϵ in the predicted range are compared with Socolofsky's data, as depicted in Figure 3-8. A value of 0.005 for ϵ gives the best agreement of modeled f vs. U_N with experimental data, and is the value used in this study.

The values of U_N used in the calibration span the range of deep-water plume types, which include Type 2 plumes with distinct peels, Type 3 plumes with overlapping, random peels, as well as Type 1* plumes with peeling dispersed phases. Therefore, buoyant detrainment is accurately predicted for multi-phase plumes in deep water, although the modeling of Type 1* plumes is speculative due to the model's inability to simulate detraining particles.

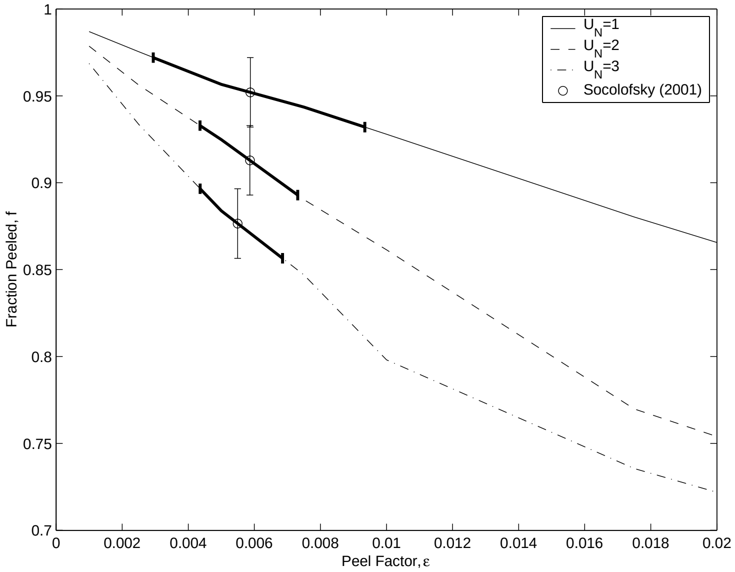

Figure 3-7: Model predicted f vs. ϵ curves for various U_N, with superimposed experimental values from Socolofsky (2001).

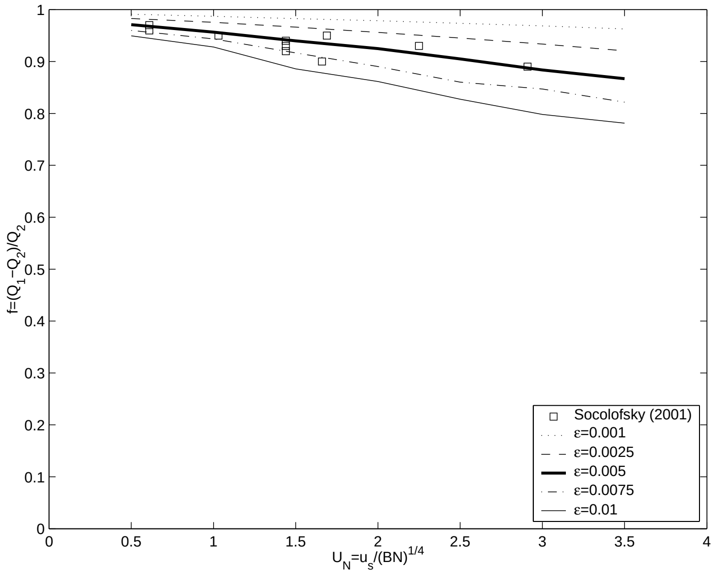

Figure 3-8: Model predicted f for different ϵ, plotted alongside experimental data. Open squares are data from Socolofsky (2001), lines are model output.

Parameter	Ascending Plume	Descending Plume
Release Depth [m]	3	0
Ceiling Depth [m]	0	3
Particle Radius [mm]	3.6	3.6
Initial Flux [L/min]	0.0751	0.0751
Linear Stratification [1/s]	0.27	0.27
Particle Density [kg/m^3]	0.001	2000
Buoyancy Flux [m^4/s$^3 \cdot 10^{-5}$]	1.23	1.23

Table 3.3: Model Parameters for basic functionality verification.

3.3 Model Functionality

In order to model negatively buoyant particles, it was necessary to invert the computer model described in Crounse (2000). While the equations described therein are general, the computer model was initially designed to work only for ascending plumes. The model was adapted to work for descending plumes in part by Brian Crounse and in part by the author. A simple test to verify successful adaptation relies on the independence of the governing fluid mechanics of plume propagation direction. In essence, equivalent magnitude releases of negative or positive buoyancy should produce plumes that differ only in the sign of the relevant fluxes. Table 3.3 lists the model parameters used to verify this property.

As can be seen in Figure 3-9, the magnitude of output from the negatively and positively buoyant model runs is virtually indistinguishable. Hence, the model is verified to function identically in either ascending or descending mode, which is a basic requirement of this study.

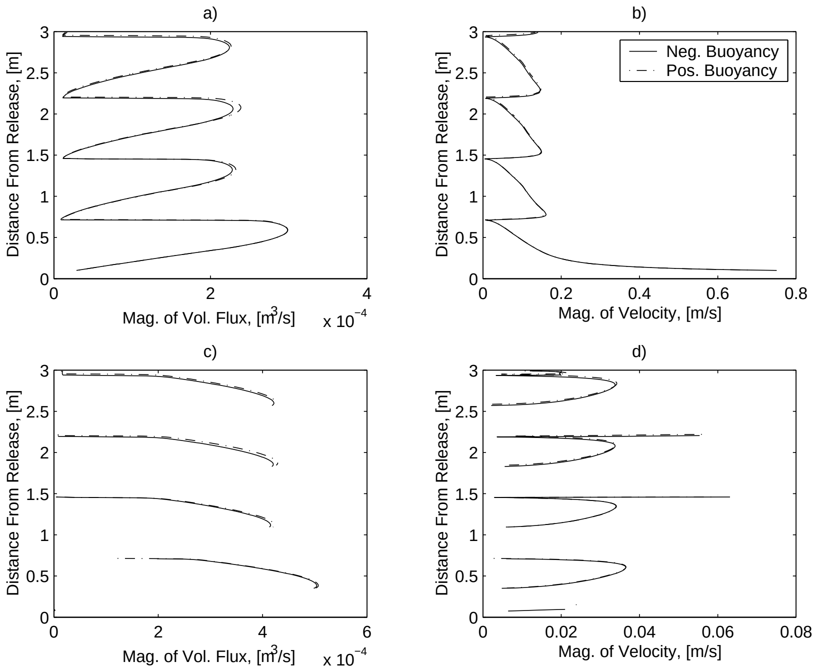

Figure 3-9: Comparison of plume model output for equal but opposite buoyancy fluxes. All variables are plotted as magnitudes for easy comparison. a) Inner plume volume flux, b) Inner plume velocity, c) Outer plume volume flux, d) Outer plume velocity.

3.4 Mass Transfer

The mass transfer coefficient introduced in Equation 2.4 is calculated by an empirical correlation based on the particle Reynolds and Schmidt numbers:

$$Re = \frac{\rho\ d_p u_p}{\mu} \tag{3.2}$$

$$Sc = \frac{\mu}{\rho\ D} \tag{3.3}$$

where d_p is the effective particle diameter, ρ and μ are the density and viscosity of the ambient fluid, and D is the diffusivity of the CO_2-seawater system. The mass transfer coefficient, then, is a function of both particle size and velocity. Crounse (2000) used a correction factor of $\lambda = 0.5$ to match the mass transfer model with data for hydrate inhibited CO_2 droplet dissolution presented by Hirai et al. (1996). Since the data from Hirai et al. (1996) are for CO_2 liquid droplets covered in a hydrate film, it is necessary to revisit the accuracy of the mass transfer correlation for a solid hydrate particle.

Preliminary data on the dissolution of solid CO_2 hydrates in the deep ocean was available from Rehder et al. (2001). Rehder et al. (2001) observed the dissolution of approximately cylindrical plugs of CO_2 hydrate, 2.2 cm in diameter and 3-4 cm in length. The plugs were placed in the ocean at a depth of 1000m, in a sample holder that permitted seawater flow around them. Observation by camera allowed linear diameter loss rates of 0.94 and 1.2 μm/s to be recorded. An approximate mass transfer coefficient can be calculated from these data as follows. First, analogous to Equation 2.4, the rate of mass loss for a cylinder is:

$$\frac{dm_c}{dt} = -\Lambda(\pi d_c^2/2 + \pi d_c h_c)K(C_s - c_i) \tag{3.4}$$

where m_c is the cylinder mass, $\Lambda = \lambda MW_{hyd}/MW_{CO_2}$, d_c is the cylinder diameter, and h_c is the cylinder height. Substituting $m_c = \frac{\pi}{4}\rho_c d_c^2 h_c$ into Equation 3.4 and separating terms gives:

$$d_c^2\frac{dh_c}{dt} + 2h_c d_c\frac{dd_c}{dt} = -\Lambda\left(\frac{2d_c^2}{\rho_p}K(C_s - c_i) - \frac{4d_c h_c}{\rho_c}K(C_s - c_i)\right). \tag{3.5}$$

The first terms on the left and right side of Equation 3.5 correspond to mass loss associated with height shrinkage. If we assume diameter and height loss to be independent (a good assumption far from the cylinder edges), then the rate of diameter loss can be found by using only the diameter loss terms in Equation 3.5:

$$\frac{dd_c}{dt} = -\Lambda\ \frac{2K(C_s - c_i)}{\rho_c}. \tag{3.6}$$

In Equation 3.6, $\frac{dd_c}{dt}$ is given by Rehder et al. (2001), Λ is used for calibration, C_s may be approximated from the model correlation value at 1000m of 78 kg/m^3, and the ambient concentration, c_i, is small and may be taken as zero. This allows K to be solved for as shown in Equation 3.7.

$$K = \frac{\rho_c}{2\Lambda\ C_s}\frac{dd_c}{dt} \tag{3.7}$$

Substituting into Equation 3.7 yields experimental K values of 6.6×10^{-6} and 8.4×10^{-6} m/s. Rehder et al.'s preliminary data indicate finite yet undetermined ambient currents. It is therefore necessary to hypothesize reasonable values for ambient current to judge model agreement with these data. Anticipated currents at 1000m depth are in the range of 0-0.1 m/s. Figure 3-10 shows the model predicted mass transfer coefficient as well as the range of coefficients predicted from Rehder et al.'s data. Although the ambient current is uncertain, Figure 3-10 indicates that the mass transfer coefficient given by the correlation agrees well if the actual ambient current fell within the lower part of the range, while the hydrate inhibited mass transfer coefficient with $\Lambda = 0.5$ matches well for high values of ambient current. In the absence of combined dissolution and current data, $\Lambda = 0.67$ will be used to give agreement with experimental data in the middle of the assumed ambient current range. This corresponds to an inhibition factor, λ, of 0.19 which is markedly lower than $\lambda = 0.5$ used by Crounse for hydrate-coated CO_2 droplets.

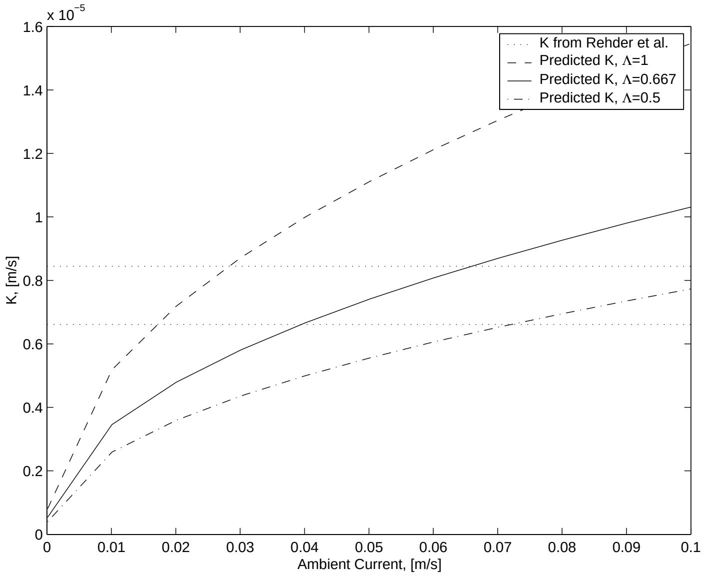

Figure 3-10: Comparison of mass transfer correlation with experimental data for different values of assumed ambient current. Dotted lines are K values calculated from Rehder et al. (2001)

Chapter 4

Modeling Results

Several different model runs have been performed to evaluate the impact of release characteristics such as particle size and mass flux on the resulting multi-phase plume. As gauges of environmental impact and sequestration efficiency, predicted pH impact and sequestration depth are of particular importance.

4.1 Particle Size Distribution

Although the method of CO_2 hydrate formation is uncertain, it is conceivable that a distribution of particle sizes will be produced instead of a single size, as described in Chapter 2. The following attempts to quantify what the impact of particle distribution might be on release characteristics.

4.1.1 Release Conditions

A CO_2 hydrate release of 34.5 kg/s, corresponding to 10 kg/s mass flux of pure CO_2 is used to compare particle distributions. Note that this release rate is around 8% of the 130 kg/s CO_2 produced by a 500 MW power plant (Herzog et al. 1997). The stratification profile shown in Figure 2-8 is used, with a release depth of 800m and a bottom depth of 4500m. Mass fractions of CO_2 hydrate were selected as shown in Figure 4-1 to approximate uniform, Gaussian, and log-normal distributions, as well as a mono-disperse base case. Although

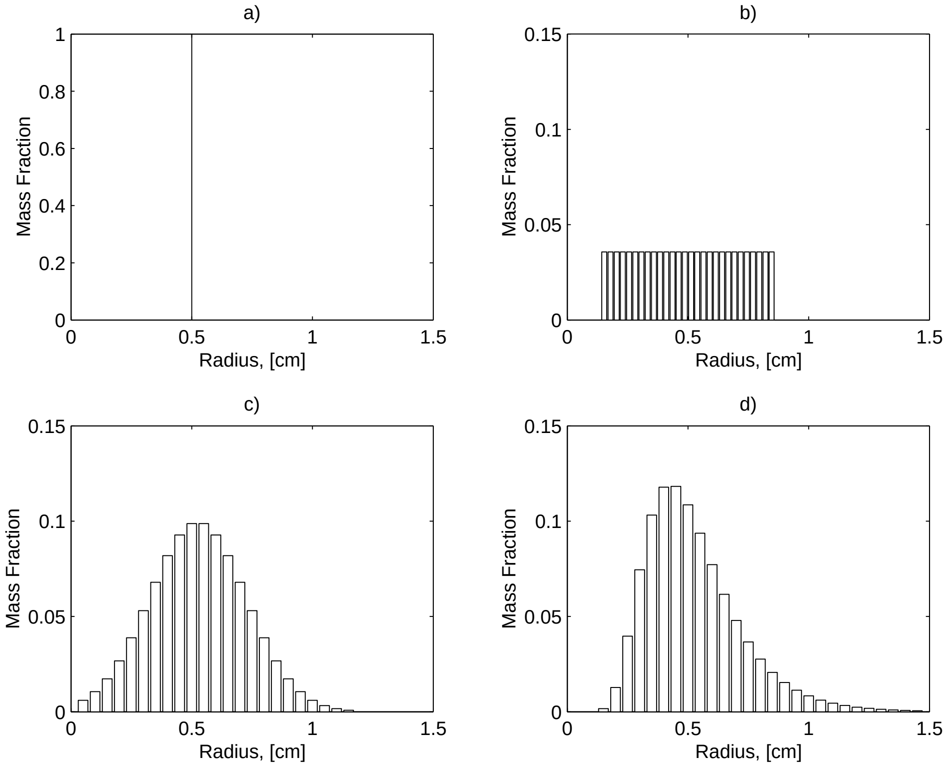

Figure 4-1: Discrete mass fraction by radius. Mean radius = 0.5 cm, standard deviation = 0.2 cm: a) Mono-disperse (standard deviation = 0), b) Uniform distribution, c) Gaussian (normal) distribution, d) Log-normal distribution.

Figure 4-1 shows the distributions for a mean radius of 0.5 cm and standard deviation of 0.2 cm, additional particle distributions with mean radii of 1.5 and 2.5 cm, and standard deviations of 0.2 cm were tested as well. The distributions tested at 0.5, 1.5, and 2.5 cm mean radius correspond to U_N of about 1.4, 2.5, and 3.1, respectively. It is hoped that by testing a range of U_N, any differences in particle distribution effect due to plume type will be indicated.

4.1.2 Plume Characteristics

The release with mean particle radius of 0.5 cm is used to illustrate local plume properties such as width, volume flux, and distribution of mass. Figures 4-2 and 4-3 show the evolution of the different plumes with depth. In general, plume width and volume flux are similar

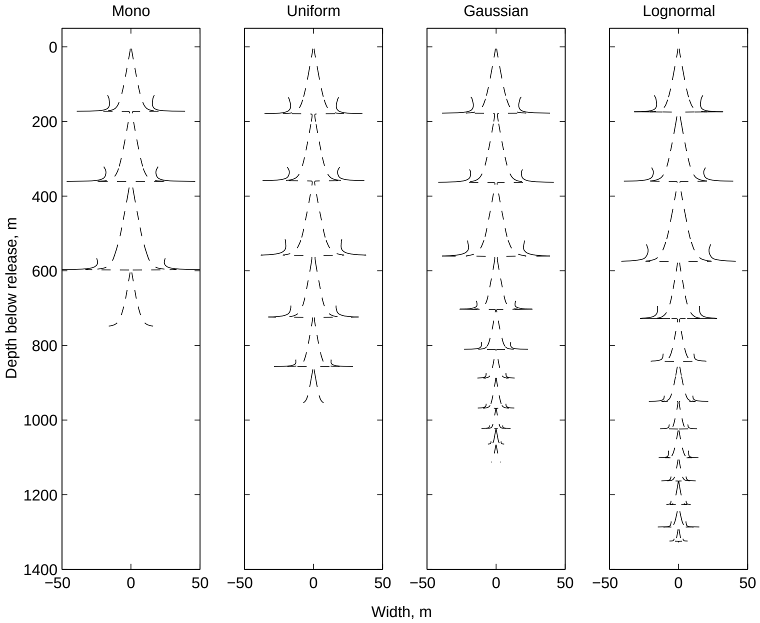

Figure 4-2: Plume width vs. depth for different particle distributions ($\mu = 0.5cm, \sigma = 0.2cm$). Dashed line is inner plume width, solid is outer.

for the three particle distributions and the mono-disperse base case over the first three peels. The particle distributions, however, indicate a tail of lower volume flux caused by the slower dissolution of larger particles. This tail effect becomes more marked when moving from uniform to Gaussian to log-normal distributions, which is a direct consequence of the amount of mass each distribution has at the highest radius particles.

Another indicator of plume differences is the amount of mass that remains in the dispersed phase as the plume propagates. Figure 4-4 shows the amount of mass contained in the dispersed phase for each distribution down to 800 meters below the release. The uniform and Gaussian distributions, with higher amounts of mass in smaller particles, show the highest initial dissolution rates. Altogether, though, the dissolution rates for all cases are similar, with most of the mass being dissolved in the first 800 meters.

Figure 4-5 gives a snapshot of the distribution of mass vs. depth for the three distributions. Most obvious in the uniform distribution is the high initial loss of mass in the smaller sized particles, although all three distributions are skewed towards larger particles as the plume propagates. Again, most of the particles are dissolved by 800 m below the release for

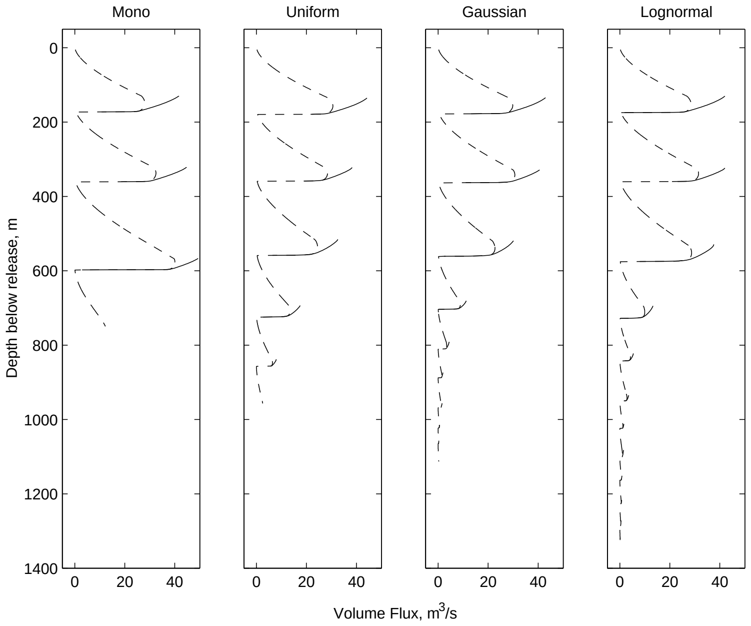

Figure 4-3: Volume flux vs. depth for different particle distributions with ($\mu = 0.5cm, \sigma = 0.2cm$). Dashed line is inner plume volume flux, solid is outer.

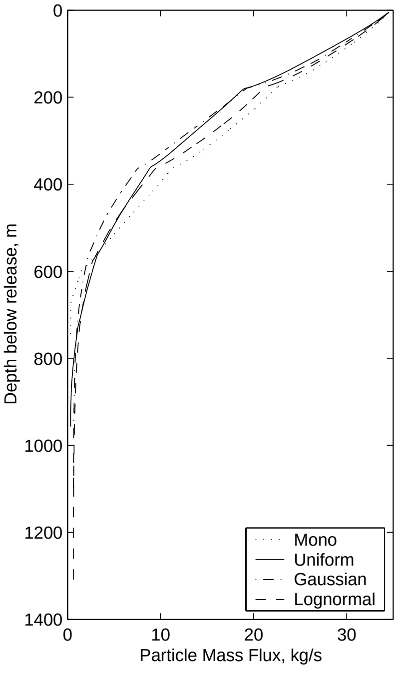

Figure 4-4: CO_2 hydrate mass flux vs. depth for different particle distributions ($\mu = 0.5cm, \sigma = 0.2cm$).

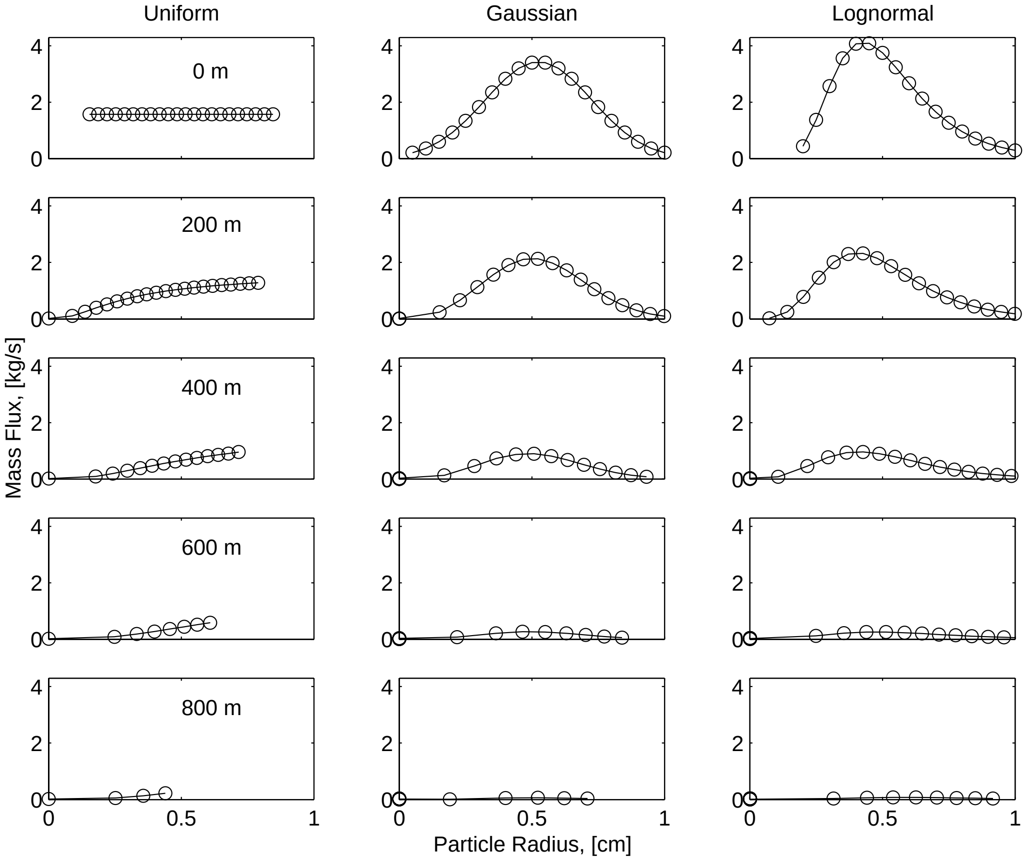

Figure 4-5: CO_2 hydrate mass flux vs. radius at various depths for different initial particle size distributions($\mu = 0.5cm, \sigma = 0.2cm$).

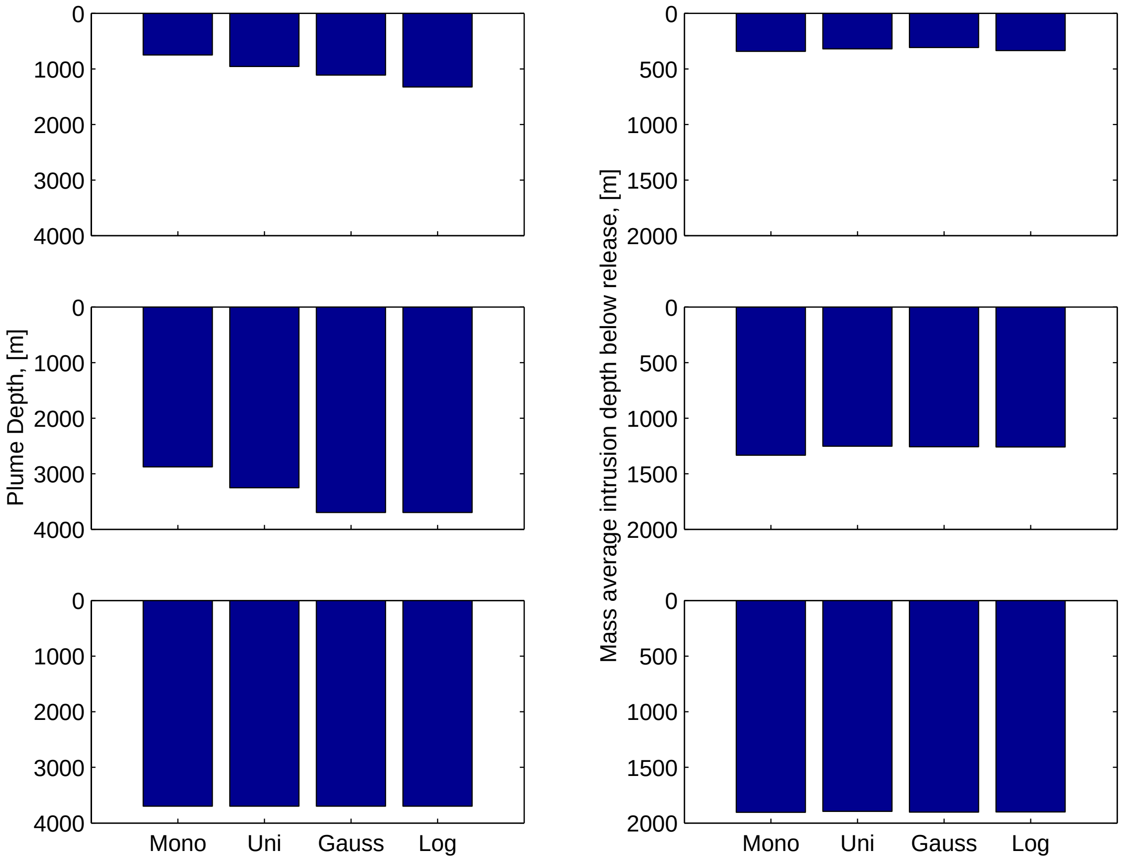

Figure 4-6: Characteristic plume depths for various particle size distributions. Top panes: $\mu = 0.5cm, \sigma = 0.2cm$. Middle panes: $\mu = 1.5cm, \sigma = 0.2cm$. Bottom panes: $\mu = 2.5cm, \sigma = 0.2cm$.

all distributions.

4.1.3 Averaged Quantities

Averaged quantities are used to effect a comparison between the sequestration depth and pH shift for each distribution. In general, the average quantities are calculated as:

$$\bar{\varphi} = \frac{\sum_{k=1}^{n} M_k \varphi_k}{\sum_{k=1}^{n} M_k} \tag{4.1}$$

where $\bar{\varphi}$ is the averaged property of interest, M_k is the mass flux in intrusion k, φ_k is the value of the property of interest in intrusion k, and n is the number of intrusions.

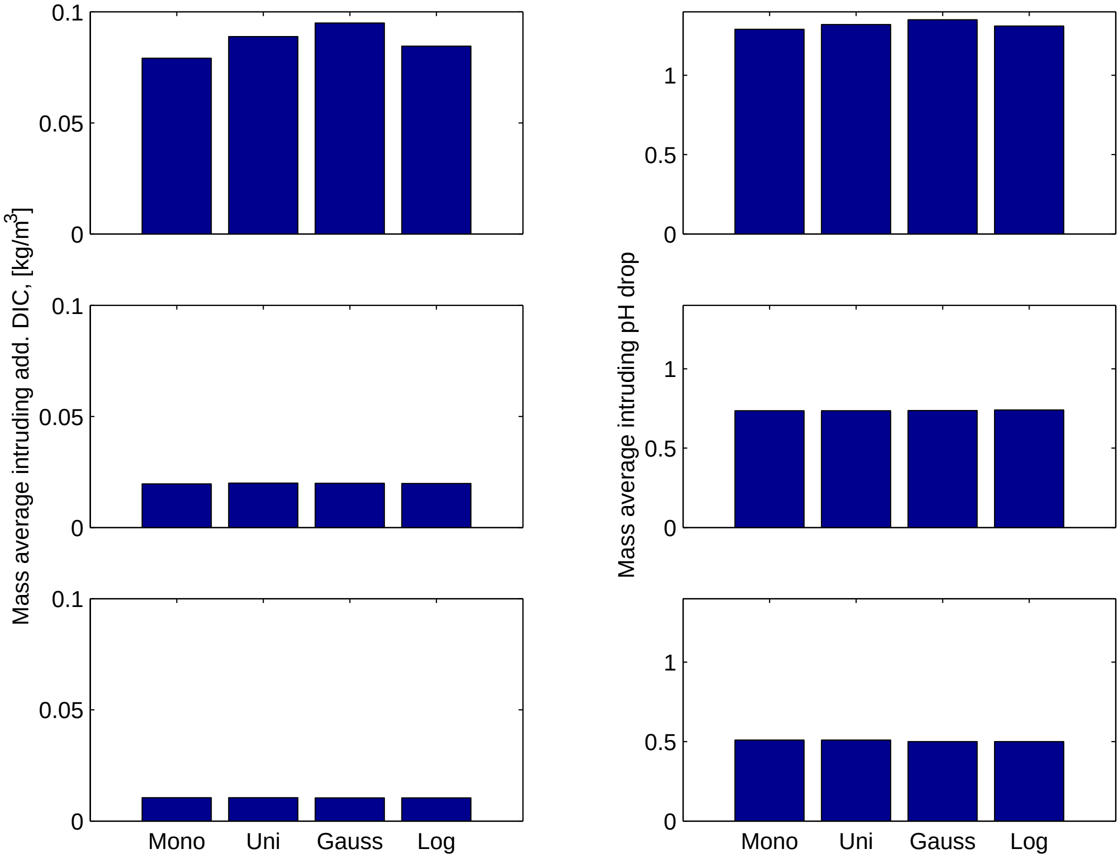

Figure 4-7: Average DIC and pH drop for plume water intruding into ambient for different particle size distributions. Top panes: $\mu = 0.5cm, \sigma = 0.2cm$. Middle panes: $\mu = 1.5cm, \sigma = 0.2cm$. Bottom panes: $\mu = 2.5cm, \sigma = 0.2cm$.

Figure 4-6 shows the plume depth and average intrusion depths for the various particle mean sizes and distributions. Plume depths for particles of a mean radius of 0.5 and 1.5 cm show some variability among the distributions due to the tails produced by larger particles. This effect is not duplicated for a mean radius of 2.5 cm as all of these plumes reach the sea-floor. Average intrusion depth shows little sensitivity to particle distribution – it is clear from Figure 4-6 that mean particle radius has a far more significant effect.

The average pH drop and DIC concentration of intruding plume water for the different particle mean sizes and distributions are shown in Figure 4-7. The distributions of mean radius 0.5 cm show some variability among the distributions, with the uniform and Gaussian distributions yielding slightly higher pH drop and DIC concentration. This is in agreement

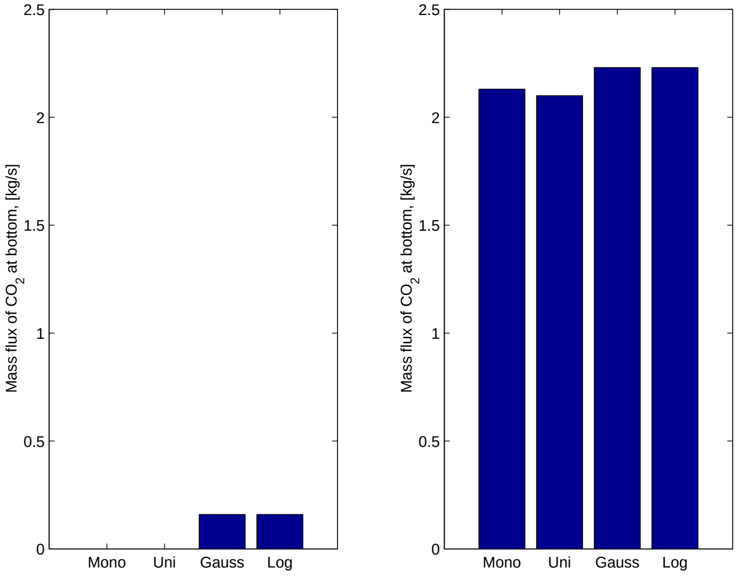

Figure 4-8: Equivalent flux of dispersed CO_2 reaching sea-floor for different particle size distributions. Left: $\mu = 1.5cm, \sigma = 0.2cm$. Right: $\mu = 2.5cm, \sigma = 0.2cm$

with the higher dissolution rates for these distributions indicated in Figure 4-4. Variability among the distributions for these parameters is barely discernible in the distributions with mean radius of 1.5 and 2.5 cm. Overall, the impact of particle distribution on pH drop and DIC concentration is small, particularly when compared with the impact of particle radius.

All of the plumes created by particle size distributions of mean 2.5 cm, and two of those with mean 1.5 cm reached the sea-floor before all CO_2 hydrate mass was dissolved. Figure 4-8 indicates the equivalent mass flux of undissolved CO_2 at the sea-floor, calculated by multiplying the mass flux of hydrate particles by the ratio MW_{CO_2}/MW_{HYD}. For a mean radius of 1.5 cm, this parameter is somewhat significant in that only the Gaussian and log-normal distributions bring undissolved mass to the sea-floor. However, the amount of mass reaching the bottom is only about 2% of the initial release, and is not enough to affect the averaged parameters described above. For the 2.5 cm mean radius case, the Gaussian and log-normal distributions bring slightly more undissolved mass to the sea-floor, but the distributions are overall comparable. Of note is the fact that for this case about 20% of the released CO_2 reaches the bottom, a property that will be explored more in the Section 4.2.

In summary, although the shape of the particle size distribution has some noticeable

Hydrate Mass Flux [kg/s]	Pure CO_2 Mass Flux [kg/s]	Diameter [cm]									
		0.5	1	1.5	2	2.5	3	3.5	4	4.5	5
3.5	1	1.6	2.5	3.2	3.8	4.2	4.4	4.7	5.0	5.3	5.5
35	10	0.90	1.4	1.8	2.1	2.3	2.5	2.7	2.8	3.0	3.11
350	100	0.50	0.79	1.0	1.2	1.3	1.4	1.5	1.6	1.7	1.8
3500	1000	0.29	0.44	0.57	0.68	0.74	0.79	0.84	0.89	0.94	0.98

Table 4.1: U_N for modeled release parameters.

effects on local plume characteristics, its impact on averaged quantities such as depth and concentration is small. Since average depth and concentration are the relevant parameters for gauging sequestration efficiency and environmental impact, releases of mono-disperse particles will be used to study design parameters such as particle radius and CO_2 hydrate mass flux in the following section.

4.2 Particle Diameter and Mass Flux

CO_2 hydrate particle diameter and mass release rate are important design parameters for the release. The effect of these parameters on plume characteristics is explored in this section.

4.2.1 Release Conditions

In order to get a broad indication of the behavior of CO_2 hydrate releases, the mass injection rate of CO_2 hydrate is varied from 3.5-3500 kg/s, corresponding to pure CO_2 rates of 1-1000 kg/s. Particle diameter is varied from 0.5-5 cm. Release parameters and corresponding U_N are shown in Table 4.1. Note that runs with U_N much less than 1.5 or much greater than 2.5 are outside of the calibrated range of the model, and hence are more speculative. The release point for all runs was 800 m, with the stratification profile and corresponding bottom depth of 4500 m as shown in Figure 2-8.

4.2.2 Plume Depth

The modeled plume depths and average intrusion depths below the release point (calculated as indicated in Section 4.1.3) as a function of particle diameter are shown in Figure 4-9 for each CO_2 mass release rate. For reference, the dissolution height of isolated, falling CO_2 hydrate particles versus particle diameter is plotted alongside the plume depths. The plume group effect, indicated by the difference between the falling particle depth and the plume depth, increases slightly with particle diameter and markedly with mass flux. Plume depth increases quite strongly with particle diameter, and to a lesser extent with mass flux. Average intrusion depth below release, perhaps an indicator of sequestration depth, follows similar trends. Generally, the average intrusion depths are favorable in that they result in CO_2 trapping far below the release, desirable for sequestration efficiency.

A plume depth of 3700 m below the release indicates that the plume has reached the bottom. As indicated in Figure 4-9, several of the release scenarios in fact did this. Figure 4-10 shows the fraction of released mass reaching the bottom vs. particle diameter for each mass flux. As follows from the plume depth predictions, the highest diameters and mass fluxes bring the most undissolved mass to the bottom. The accumulation of undissolved CO_2 hydrate mass on the sea floor is a separate transport problem that will be considered in Chapter 5.

4.2.3 DIC and pH

Figure 4-11 shows the averaged modeled intruding excess DIC and pH. As indicated in Chapter 2, pH is a nonlinear function of DIC so the curves differ somewhat in shape. A direct measure of dilution, DIC concentrations decrease strongly with diameter and increase with mass injection rate. The additional dilution created by larger mass injection rates is significant: increasing mass flux by a factor of 1000 only increases average DIC concentration by a factor of about 4. This indicates an increase in volume flux by a factor of 250. Additionally, the amount of mass reaching the sea-floor seems to have little effect on the intruding DIC concentration, as the concentration curves maintain a consistent trend between plumes that reach the bottom and those that do not. The predicted average pH values follow a similar

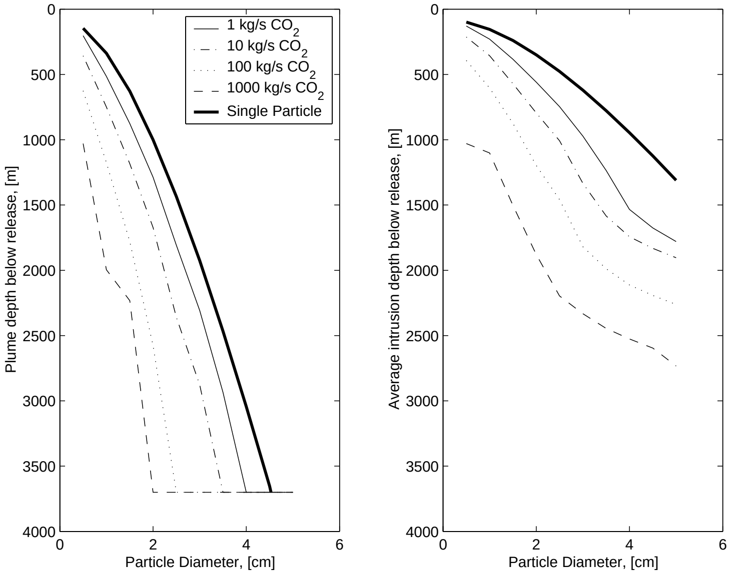

Figure 4-9: Plume depth and average intrusion depth vs. particle diameter for different CO_2 release rates. Dark solid line is dissolution depth vs. diameter for falling, isolated particles.

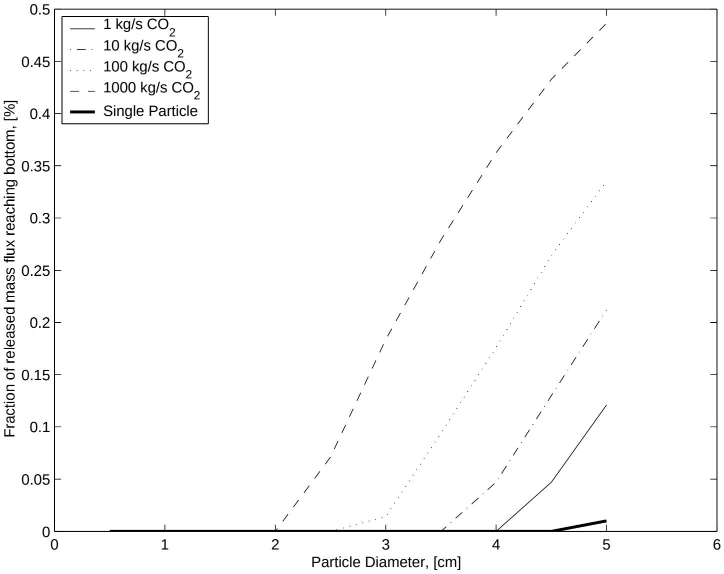

Figure 4-10: Undissolved mass reaching bottom of domain vs. particle diameter for different CO_2 release rates.

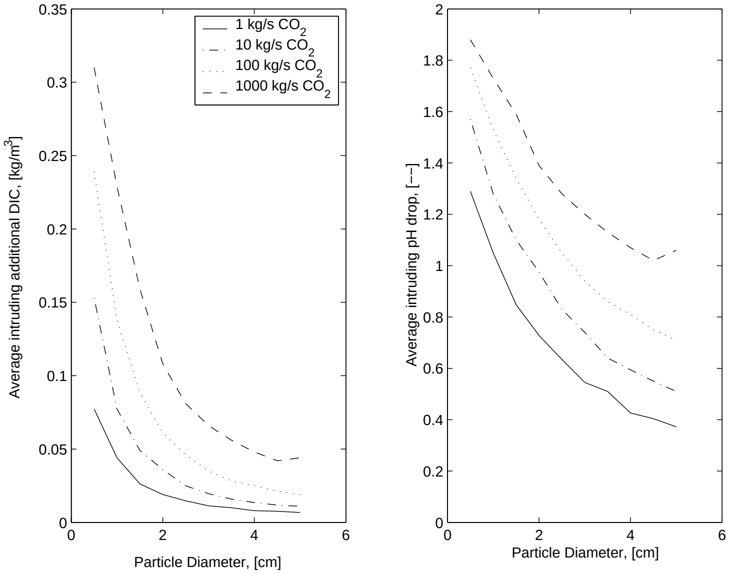

Figure 4-11: Average intruding additional DIC and pH vs. particle diameter for different CO_2 release rates.

trend to DIC concentration, with the three lowest mass rates yielding predicted pH drops of less than 1 unit for diameters greater than around 2 cm.

DIC concentration at a distance of about 1000m downstream is calculated using a simple dilution model. Okubo (1971) described the evolution of a dye patch versus time in coastal surface waters. His analysis yielded the approximate relation

$$\sigma_r^2 = 0.01t^{2.3} \tag{4.2}$$

where σ_r^2 is the radial spatial variance of dye concentration in cm^2 and t is the time in seconds. Okubu's model can be applied to the current situation, approximating that the diffusion properties at depth are similar to those in coastal surface waters. Some further assumptions about the plume and concentration field are necessary to calculate the far-field concentration. The plume is approximated as a continuous release with dimensions determined as described below.

First, the thickness of the release is taken as the plume height, and the initial concentration is taken as the depth averaged concentration, C, calculated for each release above.

This is reasonable considering that the fluctuating, turbulent nature of the plume should act to spread mass fairly evenly over its depth (the numerical model only gives average peel locations). An effective width of the plume is calculated from the concentration and height as $w = \dot{m}/hCU$, where U is the assumed ambient current of $0.05m/s$. Vertical mixing is ignored over the 1000m field of interest, given that the vertical mixing time scale of h^2/E_z is much greater than the lateral mixing time-scale of w^2/E_y, with $E_y \approx\ 10^3 E_z$. The initial variance, $\sigma_{o,r}$, can then be calculated, approximating the initial width as $3\sigma_{o,y}$ and using the relationship between σ_r and σ_y:

$$\sigma_{o,r} = \sqrt{2}\sigma_{o,y} \tag{4.3}$$

Using $\sigma_{o,r}$ and Equation 4.2, an equivalent initial time, t_o, is calculated. Using t_o and the time to reach 1000m of $t_{adv} = x/U = 20,000s$, the far field spatial variation, σ_r^2, is found by using $t = t_o + t_{adv}$ in Equation 4.2. The far-field dilution is then $\sigma_r/\sigma_{o,r}$.

Figure 4-12 shows the excess far-field DIC concentrations and pH drops for all of the modeled releases. In general, the releases of higher mass flux achieve less dilution at 1000m because more volume is required to dilute their initially large concentration fields. For instance, all of the far field DIC values for the 10 kg/s CO_2 runs are less than 3% of their near field values, whereas the far field DIC concentrations for the 1000 kg/s runs are over 20% of their near field values. This indicates a trade-off between the high near field dilution and deep penetration depth of large mass injection rates and the corresponding lower far field dilution.

4.2.4 Sensitivity to Mass Transfer Model

As indicated in Section 3.4, the mass transfer model is calibrated based on an extremely limited amount of experimental data. Hence, it is appropriate to test the sensitivity of the model outputs to the mass transfer model. In Section 3.4, a value of 0.67 for the factor $\Lambda = \left(\frac{MW_{hyd}}{MW_{CO_2}}\right)\lambda$, where λ is a correction factor accounting for CO_2 hydrate dissolution, is used to match the mass transfer model to experimental data. Λ was varied over the range 0.1 to 2 to gauge model response to changes in the mass transfer model. Note that $\Lambda = 1.7$ ($\lambda = 0.5$) correponds to the mass transfer rate reported for a hydrate-covered liquid CO_2

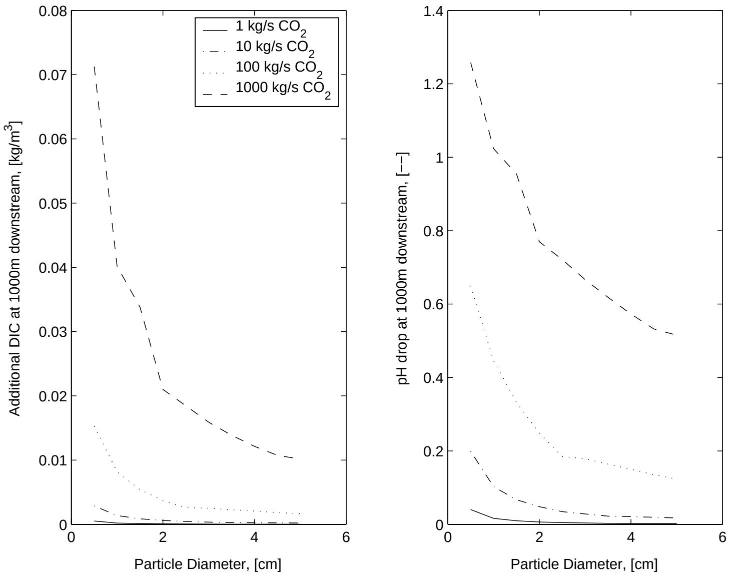

Figure 4-12: Far-field (1000m downstream) additional DIC and pH vs. particle diameter for different CO_2 release rates.

droplet in Hirai et al. (1997). As Figures 4-13-4-14 indicate, the model outputs are quite sensitive to the mass transfer model. In the range of Λ between 0.5 and 1 (corresponding best with solid hydrate dissolution data from Rehder et al. (2001)), depths differ by about 1000 m, and pH drop varies by about 0.5 units. At the lowest values of Λ, a significant portion of the dispersed phase reaches the bottom undissolved. These results underscore the need for reliable CO_2 hydrate mass transfer data to calibrate the model.

4.2.5 Implications of Ambient Current

The model used in this study makes the assumption of a stagnant ambient, although a background current of around 0.05 m/s is expected. Socolofsky (2001) performed a series of experiments to investigate the impact of ambient current on multi-phase plumes. Figure 4-16 shows the behavior of a current-dominated multi-phase plume. Of particular importance is the separation height (or depth, depending on particle buoyancy), h_s, which indicates the height at which the entrained plume water separates from the dispersed phase. The separation height of the entrained water is significant in that above that point, there will

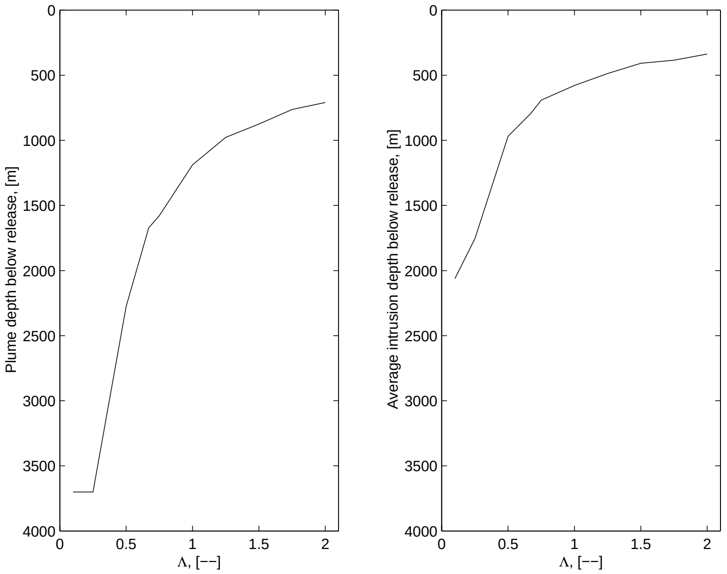

Figure 4-13: Sensitivity of plume depths to mass transfer model.

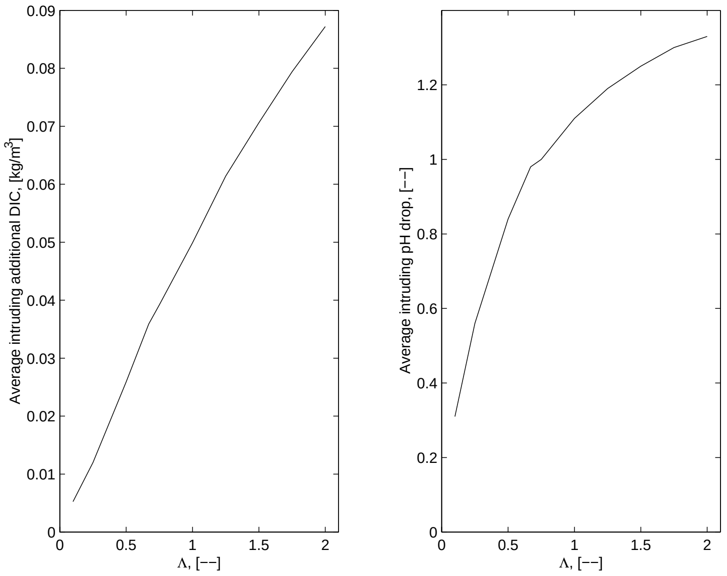

Figure 4-14: Sensitivity of average DIC and pH drop to mass transfer model.

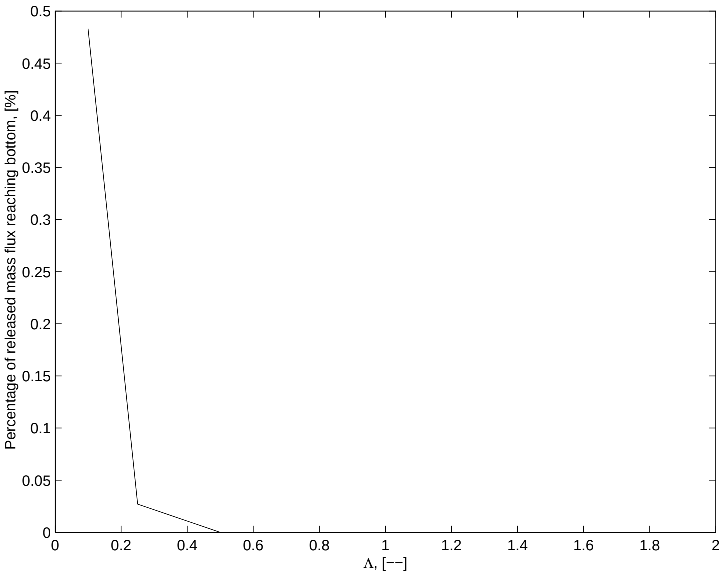

Figure 4-15: Sensitivity of undissolved mass reaching bottom to mass transfer model.

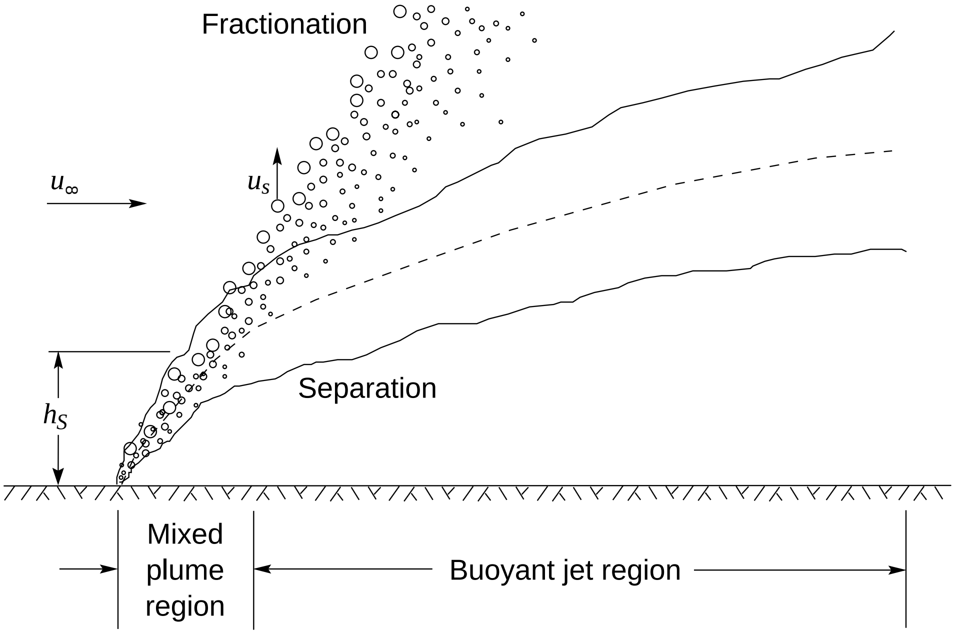

Figure 4-16: Schematic of a two-phase plume in a crossflow. Source: Socolofsky (2001).

no longer be a plume 'group effect'. Hence, current dominated plumes are expected to travel less vertical distance than stagnant plumes, having plume depths that more closely resemble those of independent, dissolving particles. From his experimental data, Socolofsky determined the correlation for h_s shown in Equation 4.4.

$$h_s = \frac{5.1B}{(u_\infty u_s^{2.4})^{0.88}} \tag{4.4}$$

where B is the buoyancy flux, u_∞ is the ambient current, and u_s is the particle slip velocity.

A heuristic indication of whether a plume is expected to be in a weak or strong current regime can be obtained by comparing h_s with the first peel trap height, h_T. It is expected that if h_T is much greater than h_s, the entrained water will separate before much of the plume group effect is realized. If the converse is true, peeling will occur before the entrained water separates and the plume group effect will be significant. h_T for the first peel of a multi-phase plume in stagnant stratification is given as (Socolofsky 2001):

$$h_T/l_c = 2.8 - 0.27U_N \tag{4.5}$$

where l_c is a characteristic plume length scale defined as $(B/N^3)^{1/4}$. Dividing Equation 4.5 by 4.4 yields an expression for the ratio h_T/h_s, which indicates strong current if it is greater than about one, and weak current if it is less than about one.

$$\frac{h_T}{h_s} = \frac{l_c(2.8 - 0.27U_N)(u_\infty u_s^{2.4})^{0.88}}{5.1B} \tag{4.6}$$

Figure 4-17 shows the relation in Equation 4.6 plotted for the various CO_2 mass fluxes and CO_2 hydrate particle diameters used in the model runs, with the dark dashed line indicating the approximate separation between weak and strong current regimes. From the figure, it is clear that as mass flux increases and particle radius decreases, current is expected to have a less significant effect. All plumes created with a CO_2 mass flux of 1 kg/s are expected to be influenced by ambient current, with the 10 kg/s runs at the higher diameter indicating some effect, and the 100 and 1000 kg/s runs expected to show relatively little sensitivity to current. The dependence of current influence is somewhat convenient

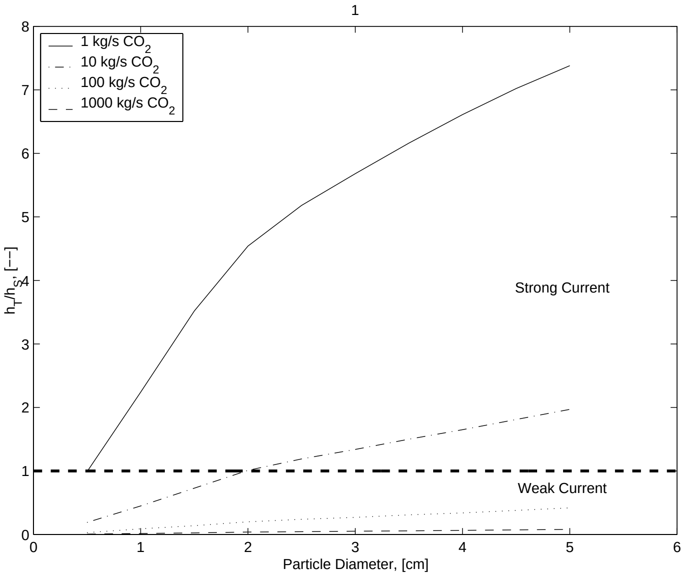

Figure 4-17: Comparison of trap and separation heights for modeled fluxes and diameters.

in that the plumes that are expected to benefit most from the plume group effect are least sensitive to ambient current. This heuristic examination should be taken as a rough view of ambient current effects, subject to further experimental validation. The release properties of a current dominated plume are explored in Chapter 5.

4.2.6 Comparison of Positive and Negative Buoyancy

A unique characteristic of CO_2 hydrate particle plumes is the positive feedback between the negative buoyancy imparted by dissolving CO_2 and the falling plume water. An approximate look at the importance of this effect is taken by looking at the plume group effect for releases of dissolving CO_2 particles of equal but opposite buoyancy. This is accomplished by examining modeled plume heights or depths (called distances hereafter) for both positively and negatively buoyant particles of varying initial diameter.

Both sets of particles are given the composition of CO_2 hydrates. The negatively buoyant particles have a density equal to that of CO_2 hydrates, while the positively buoyant particles have a density calculated such that the difference in particle and ambient density at the release point is equal but opposite that of the negatively buoyant particles. These particle

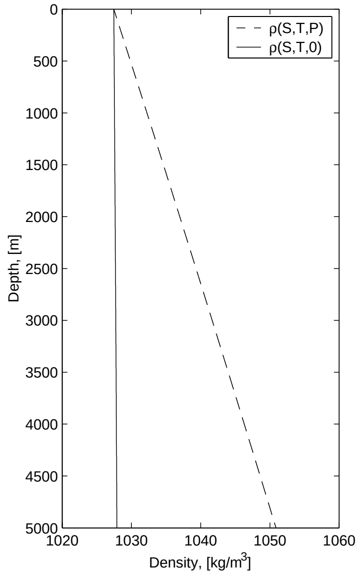

Figure 4-18: Linear stratification profile for buoyancy comparison runs. $N = 0.007$.

densities, combined with a constant volumetric injection rate of 10 L/s, give both particle releases an equal but opposite initial buoyancy flux, B. A linear stratification profile with $N = 0.007s^{-1}$, shown in Figure 4-18, is used to reduce any directional effects due to stratification. This profile was obtained by linearizing the profile shown in Figure 2-8 around the value at 2000 m. The particles are released at a depth of 2000 m where the ambient density at pressure is $1037kg/m^3$. This yields a density of $974kg/m^3$ for the positively buoyant particles based on the negatively buoyant hydrate particle density of $1100kg/m^3$.

Figure 4-19 shows characteristic distances and distance ratios versus diameter for the two release types. Of first note is that the single particle dissolution distance has a slight directional dependence due to particle velocity and mass transfer correlations scaling with the magnitude of density. However, modeled differences in falling and rising particle distance range from 7 to 10% and do not account for the large differences in plume distance. The negatively buoyant plumes travel from 17 to 91% further than the positively buoyant ones.

The right pane of Figure 4-19 shows the ratio of plume distance to particle dissolution distance, a parameter that should be less sensitive to differences in falling and rising particle dissolution distances. The distance ratio for falling particles is higher than that for falling particles, though the magnitude changes with particle size: the ratio is 10% higher for the largest particles compared with about 70% higher for the smallest particles. For both positive and negative buoyancy, the distance ratio decreases as the particle size increases. Essentially, as particle diameter is increased, the plume characteristics are dominated more by the fast moving particles than the group effect.

This trend was indicated in Crounse (2000) as well, who found a similar increase in distance ratio with decreasing diameter for hydrate covered CO_2 liquid droplets. For a CO_2 droplet of 0.5 cm diameter, a release of 1.1 L/s, and ambient stratification of $N = 0.003s^{-1}$, Crounse calculated a distance ratio of about 2. This is lower than the value of about 4 calculated herein for positively buoyant hydrate particles. The reasons for this discrepency are two fold. First, Crounse's release conditions correspond to $U_N = 2.4$ versus $U_N = 1.1$ for the present study. Plume heights are a decreasing function of U_N as indicated in Socolofsky (2001). Second, hydrate particles are only about 30% CO_2 and so impart less negative buoyancy per mass than pure CO_2. Hence, a hypothetical release of rising hydrate particles experiences less "drag" due to the density increase in plume water than a pure CO_2 release does.

Overall, it is reasonable to conclude that differences in the density effect feedback between rising and falling CO_2 particle plumes have a significant effect on the magnitude of the plume group effect.

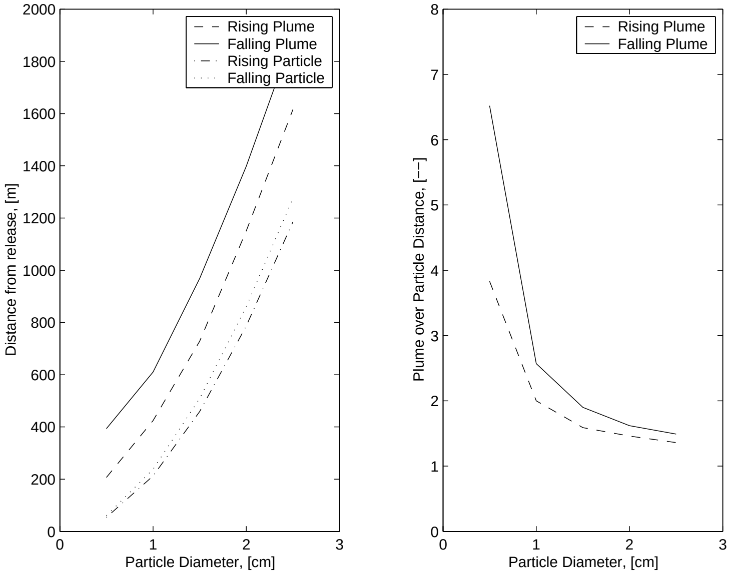

Figure 4-19: Comparison of plume and single particle distances for buoyancy comparison runs. Left pane: Single particle dissolution distance from release and plume distance from release for negative (falling) and positive (rising) buoyancy. Right: Ratio of plume distance to particle dissolution distance for positive and negative buoyancy.

Chapter 5

Comparison of Release Scenarios

As previously mentioned, the two most important aspects of an ocean CO_2 release are its environmental impact (judged by the induced pH shift), and its sequestration depth.

Since CO_2 hydrate plumes descend significant distances below the release point, they have a distinct advantage in terms of sequestration depth. However, depending on the requirements for sequestration depth, other strategies may be more attractive based on environmental impact and cost.

There are several strategies for achieving the dilution necessary to make ocean CO_2 sequestration an environmentally sound process. These strategies can be categorized in terms of the spatial dimension over which they initially spread the CO_2 release. A CO_2 hydrate or liquid CO_2 plume achieves significant spread in the vertical direction. A release from a ship-based towed pipe achieves spread in the longitudinal (parallel to the dominant advection) direction. Finally, a sea-floor mounted or floating manifold creates spreading in the lateral (perpendicular to the dominant advection) direction.

Table 5.1 is a matrix of possible CO_2 injection methods based on buoyancy and the di-

	Single Plume	Towed Pipe	Manifold
Positive Buoyancy			X
Negative Buoyancy	X	X	

Table 5.1: Options for Ocean CO_2 injection. Preferred techniques indicated with an X.

lution options listed above. For each type of release a preference is indicated. For a single plume release, negative buoyancy is preferred as it yields a larger plume length and a deeper sequestration depth. For a towed pipe release, negative buoyancy is preferred because it yields a deeper sequestration depth. Finally, a sea-floor mounted manifold injecting positively buoyant CO_2 is preferred, because a manifold based release of negative buoyancy is impractical.

The following sections compare the preferred techniques in terms of pH impact. Using the same parameterization of lateral mixing and an injection rate of $100 kg/s\ CO_2$, the scenarios are compared using the evolution of the average pH shift over a ten hour period, and the volume of water in a given pH range after ten hours.

5.1 Hydrate Particle Plume

As demonstrated in Chapter 4, the particle diameter and mass flux are the major determinants of plume characteristics. For the purposes of comparison, a 354 $kg/s\ CO_2$ hydrate (100 $kg/s\ CO_2$) release of 2.5 cm diameter particles at 800 m depth in water of 4500 m depth is used. As modeled, this release spans the entire water column without sending undissolved mass to the bottom. Figure 5-1 shows a schematic of the release.

The dilution model is the same as that presented in Section 4.2.3. The ambient current speed is taken as spatially uniform and steady with a magnitude of 5 cm/s, and vertical diffusion is neglected. The average pH shift is calculated as a function of time, equivalent to the distance downstream divided by the ambient current speed. This approach gives a sense of the pH impact felt by a passive organism advecting downstream with the plume water. The average excess carbon concentration, from which pH may be calculated, is approximated as:

$$DIC_{avg} = \frac{\dot{m}}{3\sigma_y(t) h u_a} \tag{5.1}$$

where $\dot{m}$ is the release in kg/s, $\sigma_y(t)$ is the lateral spatial standard deviation of the concentration calculated as in Section 4.2.3, h is the plume depth in m, and u_a is the ambient current velocity in m/s. As shown in Figure 5-2, the pH drop is about 0.1 after 10 hrs

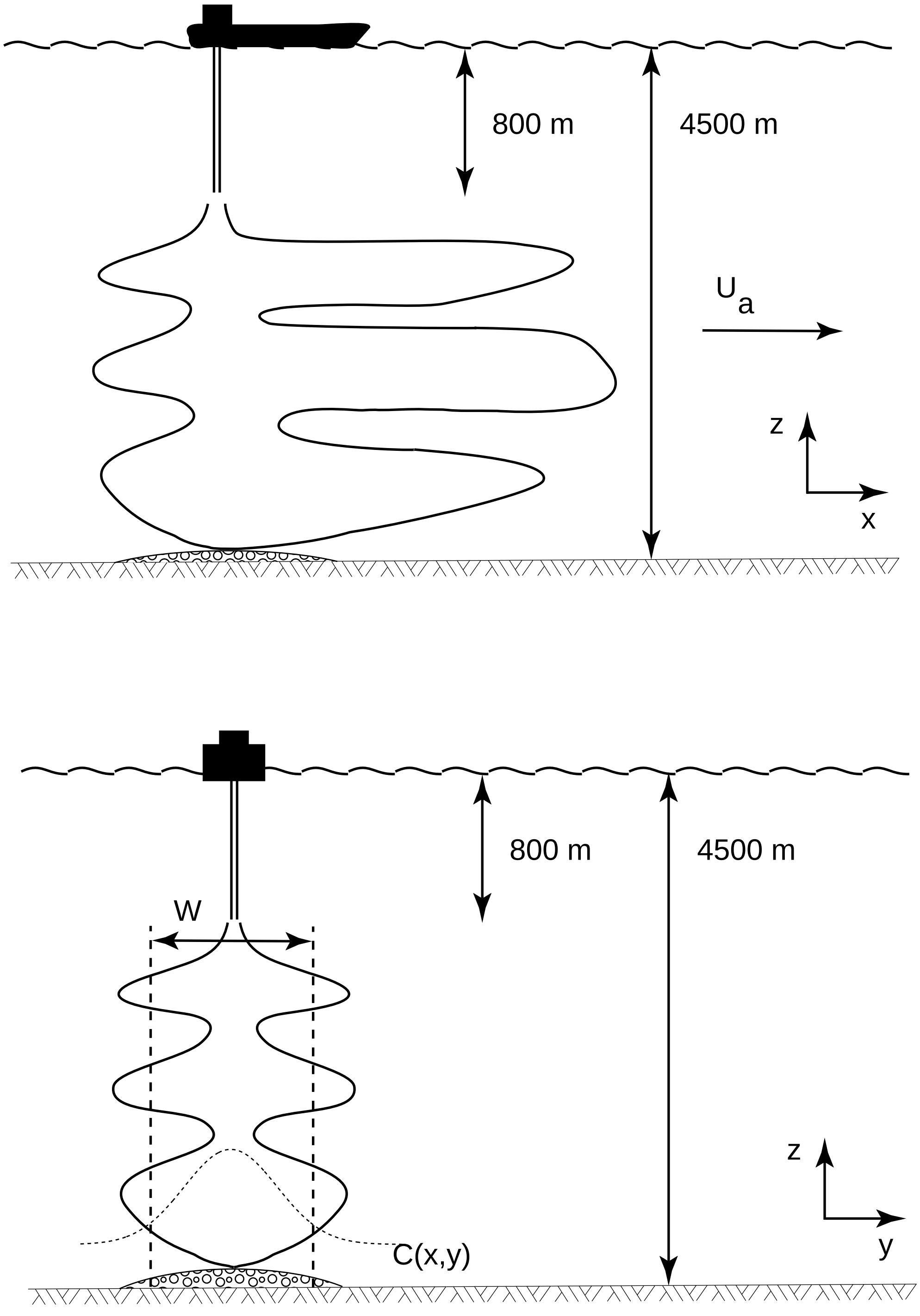

Figure 5-1: Schematic of a hydrate particle release. Not to scale.

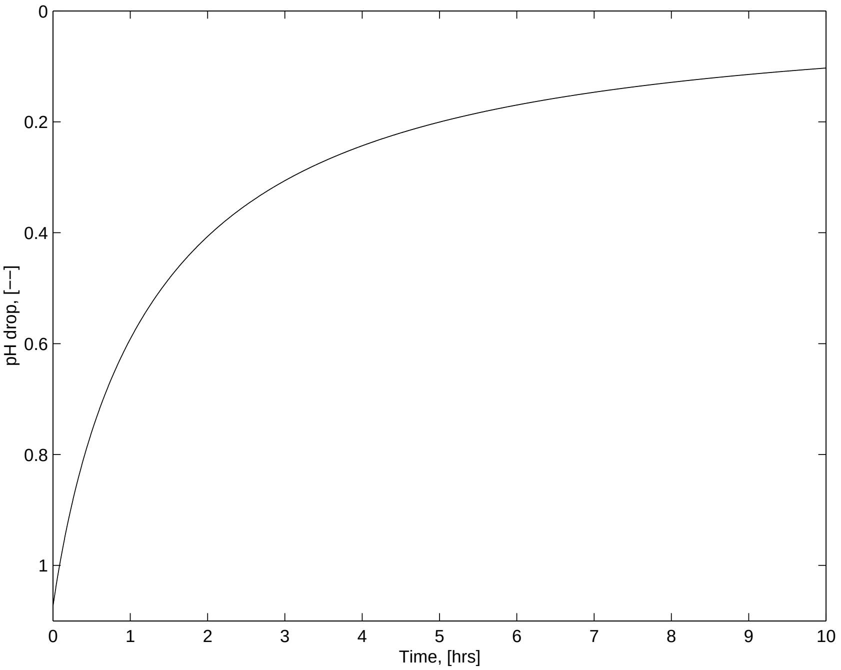

Figure 5-2: pH drop traveling downstream from a hydrate plume as a function of time.

(corresponding to a downstream distance of 1.8 km).

Another measure of impact is the volume of water at different pH levels produced by the plume. With the excess DIC cloud approximated as a Gaussian distribution as above, excess DIC concentration may be calculated as a function of time and lateral distance, y:

$$DIC(t, y) = \frac{\dot{m}}{\sqrt{2\pi} h u_a \sigma_y(t)} \exp \frac{-y^2}{2\sigma_y^2(t)} \tag{5.2}$$

where $\sigma_y(t)$ is calculated as described previously. Equation 5.2 may be solved for the lateral coordinate of a given excess DIC concentration:

$$y = \sigma_y(t) \sqrt{-2 \ln \frac{DIC}{C_c(t)}} \tag{5.3}$$

where $C_c(t) = \frac{\dot{m}}{\sqrt{2\pi} h u_a \sigma_y(t)}$. Equation 5.3 allows the width of a given concentration contour, $b = 2y$, to be calculated for each time. The volume of water with concentration greater than

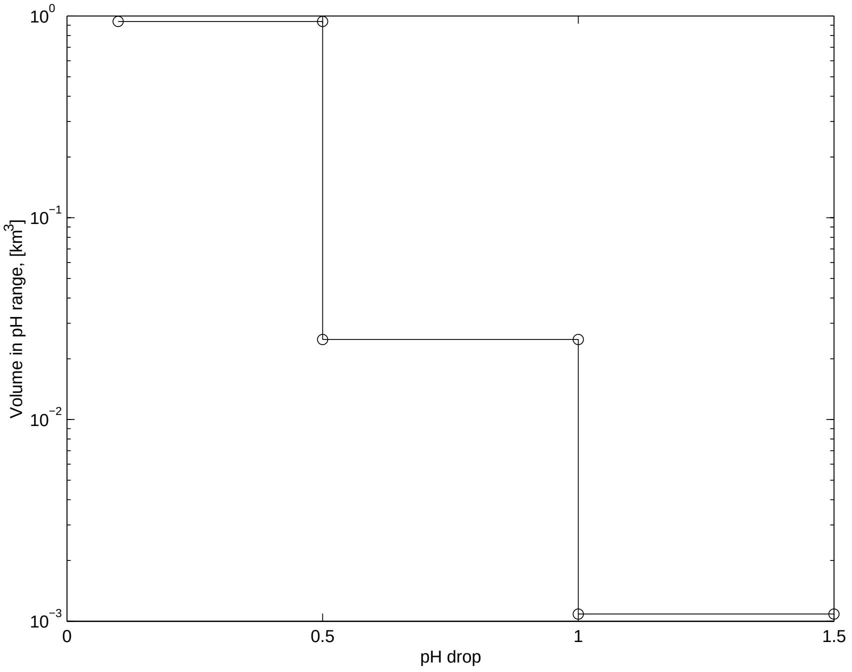

Figure 5-3: Volume of water at different pH drop ranges produced by a hydrate plume. Plotted points represent pH ranges: $0.1 < \Delta pH < 0.5, 0.5 < \Delta pH < 1.0, 1.0 < \Delta pH < 1.5$.

or equal to a given excess DIC concentration is then:

$$V(DIC) = h\int_0^x b(x'/u)dx' \tag{5.4}$$

where the equation is framed in terms of downstream distance, x, by substituting $t = x/u$. Equation 5.4 can be solved numerically for a few DIC values. Figure 5-3 shows the predicted volume of water at different ranges of pH drop produced by a CO_2 hydrate plume. There is a large volume of water produced in the fairly low pH drop range between 0.1 and 0.5 units. A comparatively smaller volume of water is produced with impact greater than 0.5 pH units.

5.1.1 Undissolved Mass Reaching Sea Floor

One element of hydrate plumes that remains unexplored is the impact of undissolved CO_2 hydrate particles accumulating on the sea floor. The problem is modeled similar to the analysis of a deep CO_2 lake presented in Herzog & Adams (1996). A mass flux of 177 kg/s of 1 cm diameter CO_2 hydrate particles, corresponding to 50 kg/s pure CO_2 release, is assumed to reach the bottom. This is 15 kg/s pure CO_2 more than the most mass reaching $4500m$ depth for the 100 kg/s pure CO_2 runs in Chapter 4, and so represents a 'worst case' scenario. To estimate the steady state size of the resulting mound, the mass flux of hydrate particles, $\dot{m}$, is equated with the mass flux from the mound due to dissolution, ΛAkC_s, allowing A, the surface area of the mound, to be solved for. The mass transfer coefficient, k, is approximated as that for $1cm$ diameter hydrate particles in an ambient current of $5cm/s$, yielding a value of $1.67 \times 10^{-5} m/s$. Λ is set to 0.67 as described previously, and C_s is given a representative value of 78 kg/m^3. This gives a steady state surface area of about $0.2km^2$ Assuming a circular surface area of the mound allows a radius to be calculated, and, for the purposes of transport modeling, the mound is broken up into a series of finite width line sources each perpendicular to the ambient current. The excess concentration field produced by each line source, j, is modeled as:

$$DIC_j(y,z,t) = \frac{\dot{m}_j}{2b_j u_a \sqrt{4\pi E_z t_j}} \exp\frac{-z^2}{4E_z t_j}\left[erf\left(\frac{y+b_j/2}{\sqrt{2}\sigma_{y,j}(t_j)}\right) - erf\left(\frac{y-b_j/2}{\sqrt{2}\sigma_{y,j}(t_j)}\right)\right] \quad (5.5)$$

where b_j is the initial width of line source j, E_z is the vertical diffusion coefficient within the benthic boundary layer, taken as constant and equal to $0.01m^2/s$ as in Herzog & Adams (1996), $\sigma_{y,j}(t)$ is the spatial standard deviation for line source j calculated as above, and t_j is the time relative to the initial position of each line source, $t_j = t - x_j/u_a$. The initial spatial standard deviation, $\sigma_{yo,j}(t)$, is approximated as $b_j/3$. The exponential factor is introduced to account for vertical diffusion. Superposing all of the line sources yields the predicted excess carbon concentrations downstream of the mound. An approximate average concentration can be found by superposing $DIC_{avg,j} = \frac{\dot{m}_j}{u_a \sigma_{y,j}(t)\sqrt{2E_z t_j}}$ for all j. Figure 5-4 shows the predicted average pH drop downstream of the mound as a function of time, traveling with the excess DIC cloud. The magnitude of the average shift is comparable to that of the pure plume release; however, the hydrate pile benefits less from lateral dilution. Overall, the creation of a particle mound is not expected to have any substantial benefits or adverse effects on the water column over those of a particle plume. However, the impacts of the mound on the

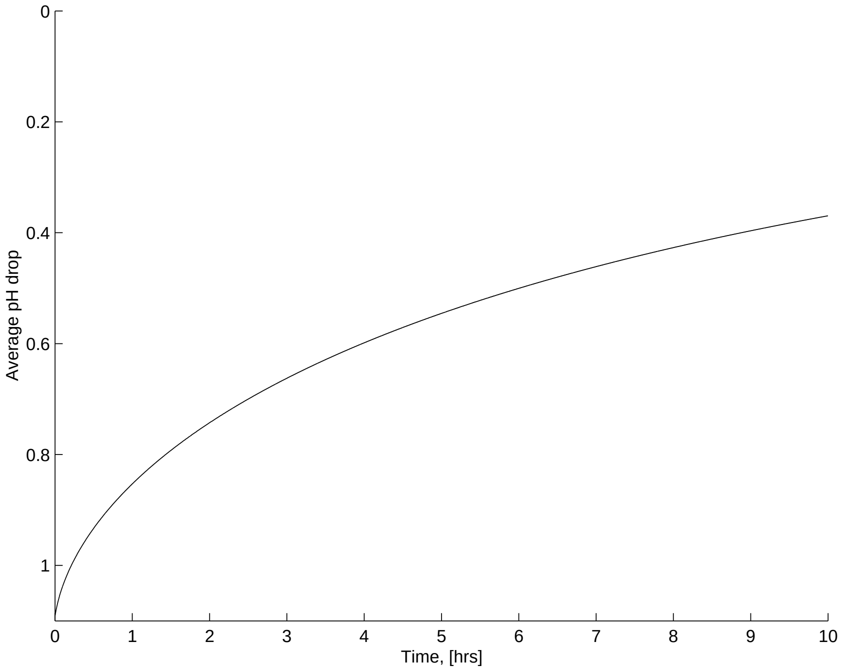

Figure 5-4: Average pH drop traveling downstream from a CO_2 hydrate mound as a function of time.

benthic community could be quite significant.

5.2 Ship-based Release

A ship-based release is envisioned as a towed pipe releasing $354kg/s$ of CO_2 hydrates ($100kg/s$ of CO_2) at a depth of $800m$. The ship velocity, set at 3 m/s, is a possible design variable to optimize dilution. The wake effect from the pipe, mentioned in Caulfield (1996), is ignored because the particles sink below the pipe, unlike a liquid CO_2 release. The ship trajectory is assumed to be straight, perpendicular to the prevailing current, and infinite in extent, neglecting any large scale circulation or Coriolis effects. Figure 5-5 shows the release schematically.

The particle sinking depth is calculated based on isolated, falling particles with a mass transfer model as presented earlier, except with the ambient current velocity of $5cm/s$ included in the magnitude of velocity used for mass transfer coefficient correlations. Note

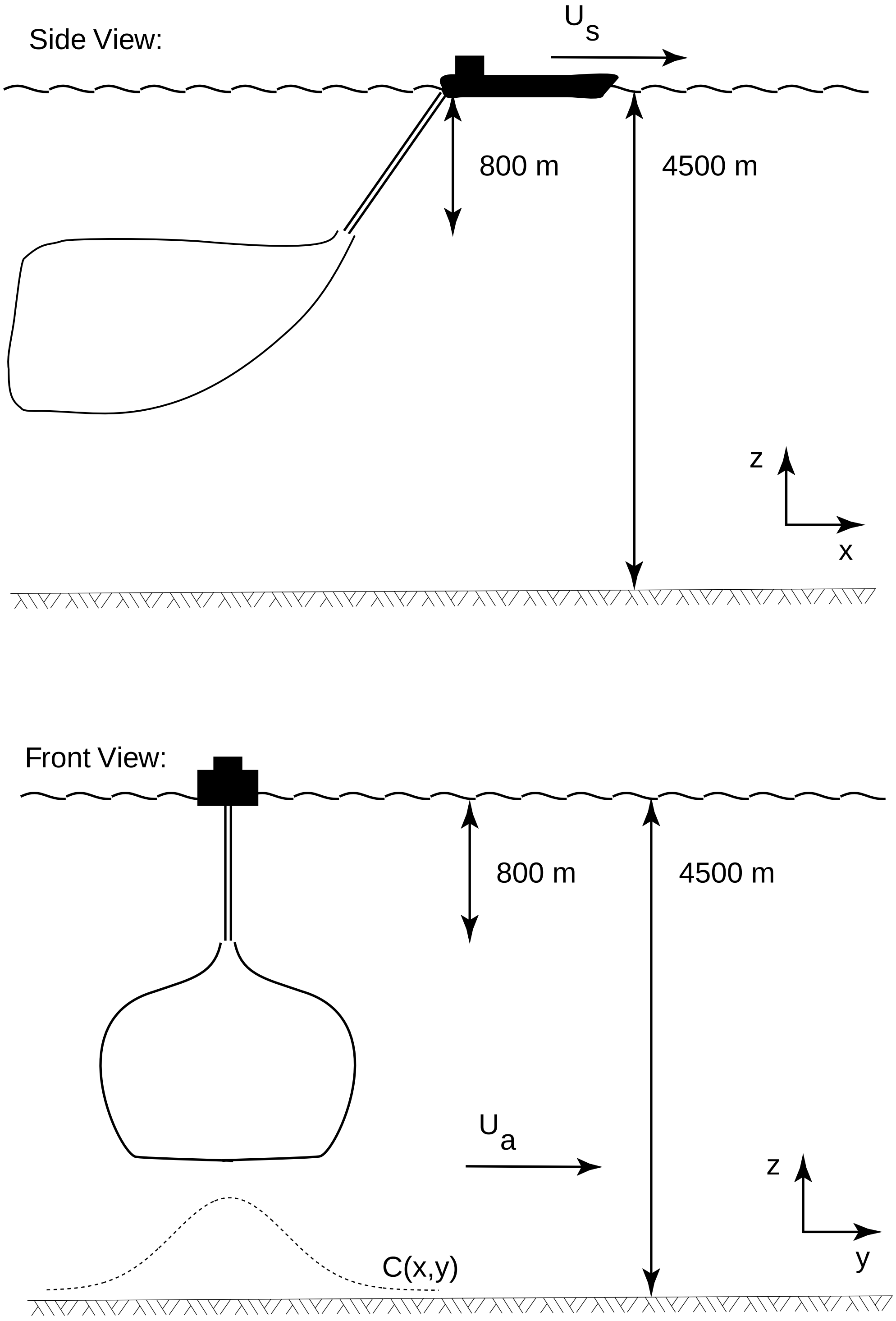

Figure 5-5: Schematic of a ship based release. Not to scale.

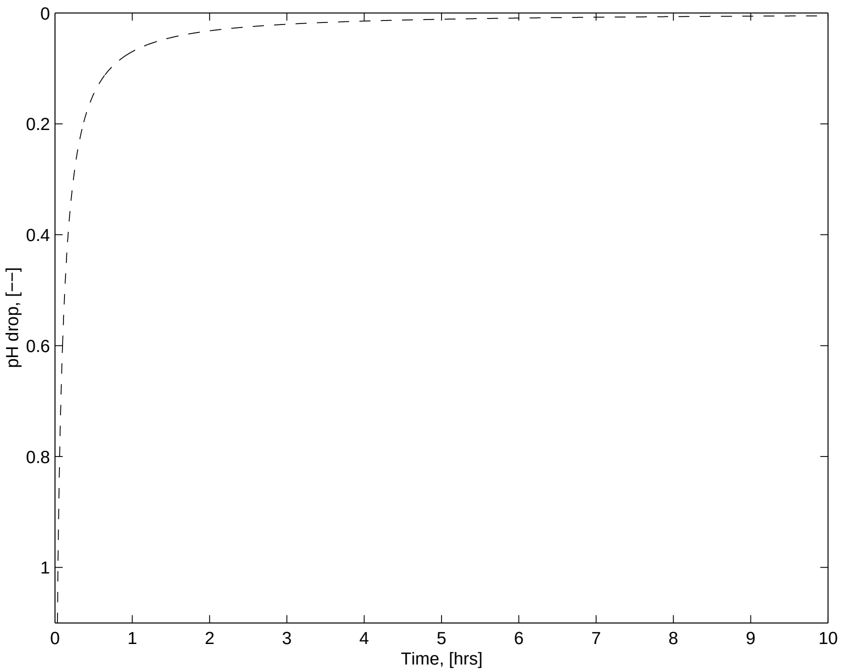

Figure 5-6: pH drop traveling away from a towed pipe as a function of time.

that, due to drag, the particles move at the ship velocity for a negligible amount of time, so that the ship velocity does not affect particle dissolution. A particle dissolution depth below release of $1390m$ for particles of $2.5cm$ diameter is found. Particle dissolution over the depth is assumed to be uniform for the purpose of dilution modeling. The average excess DIC concentration as a function of time downstream from the ship can be calculated as in Section 5.1:

$$DIC_{avg} = \frac{\dot{m}}{3\sigma_y(t)hU_S} \tag{5.6}$$

where U_S is the velocity of the ship, and the calculation of $\sigma_y(t)$ has been demonstrated previously. The initial lateral variance, $\sigma_{y,o}$, is taken conservatively as zero. Figure 5-6 shows the predicted average pH drop traveling away from the ship, or at a stationary point, depending on the frame of reference. The pH drop is initially significant due to the low initial dilution, but falls close to ambient levels fairly quickly due to the large value of U_s.

The volume of water in different pH ranges can be calculated similarly to the method used for a hydrate plume, with the exception that U_S is substituted for u_a. This yields the

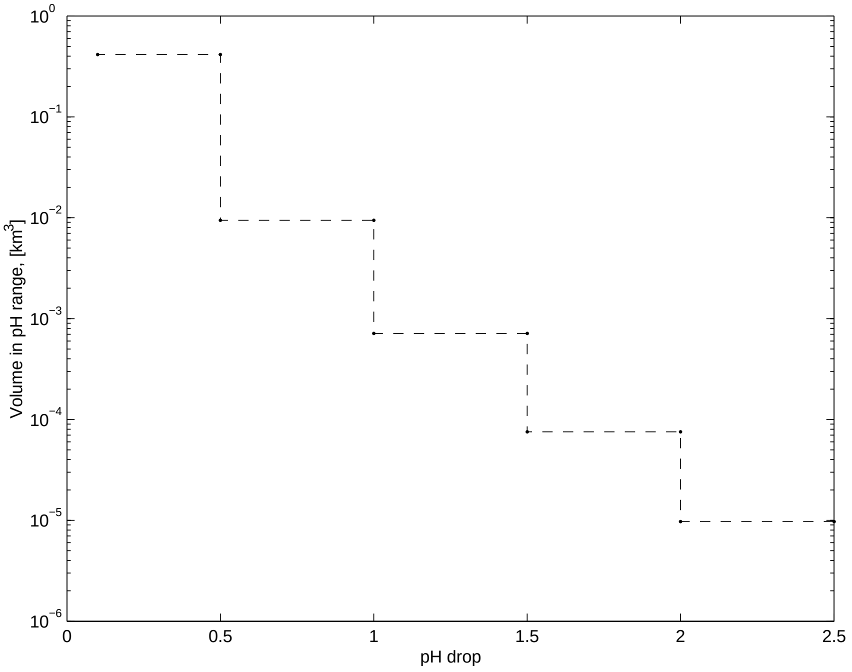

Figure 5-7: Volume of water at different pH drop ranges produced by a towed pipe. Plotted points represent pH ranges: $0.1 < \Delta pH < 0.5, 0.5 < \Delta pH < 1.0, 1.0 < \Delta pH < 1.5, 1.5 < \Delta pH < 2.0, \Delta pH > 2.0$.

predictions shown in Figure 5-7. Although there is some volume of water at the high pH drops, a comparatively large volume of low impact water is produced.

5.3 Bottom Manifold Release

A bottom manifold release could be achieved with a pipeline extending on the sea-floor to $800m$ depth and beyond. The pipeline is modeled as perpendicular to the uniform ambient current of $5cm/s$. In this case, $100kg/s$ of liquid CO_2 would be injected, resulting in rising plumes. For modeling purposes, the height of the plumes, h, and the length of the manifold, L, are considered design variables. In other words, it is assumed that droplet size and individual diffuser mass flux can be varied to spread the CO_2 evenly over a given h and L, within a reasonable limit. In practice, h is limited to $400m$ due to the volatilization of CO_2 at about $400m$ depth, whereas L might primarily be limited by pipeline cost. A value of

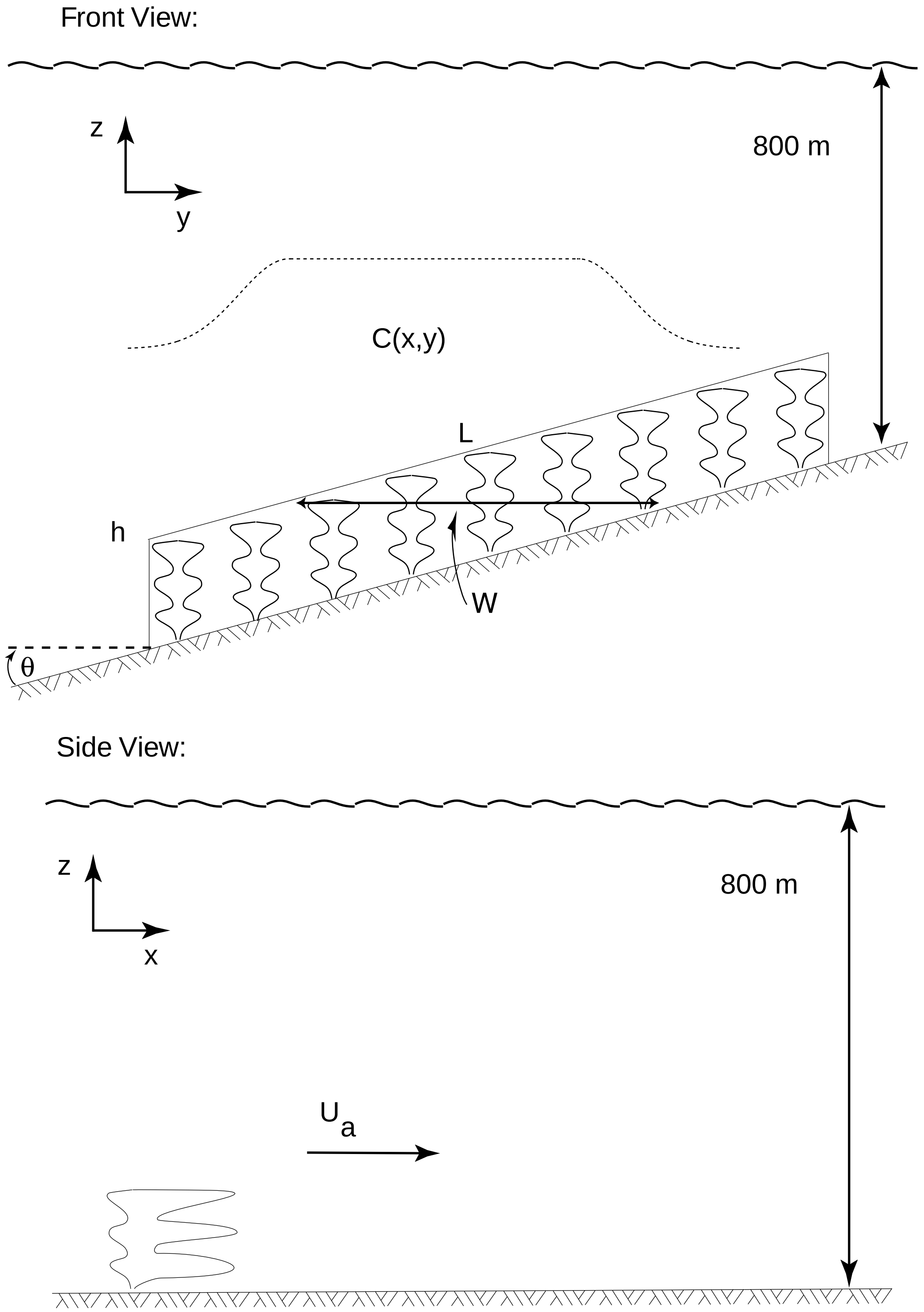

Figure 5-8: Schematic of a sea-floor manifold release. Not to scale.

$250m$ is taken for h as a compromise between sequestration depth and dilution. L is taken as half of the pipeline length required to reach $800m$, L_o. For the assumed sea-floor slope of 5 degrees, L_o is about $9000m$; therefore, L is taken as $4500m$. See Figure 5-8 for a schematic representation of a sea-floor manifold release.

The manifold system results in a rectangular source of height h, length L, and initial excess DIC concentration, $DIC_o = \dot{m}/(hLu_a)$. However, the lateral diffusion of the resulting cloud is scaled on the lateral width of the source, $w = h/\tan\theta$ where θ is the slope of the sea-floor. The system is modeled as a finite width and depth plane source with vertical diffusion neglected:

$$DIC(y,t) = \frac{\dot{m}}{2Lhu_a}\left[erf\left(\frac{y+w/2}{\sqrt{2}\sigma_y(t)}\right) - erf\left(\frac{y-w/2}{\sqrt{2}\sigma_y(t)}\right)\right] \tag{5.7}$$

where $\sigma_y(t)$ is calculated as previously, with an initial value of $w/3$. An approximate average concentration as a function of time downstream is given as $DIC_{avg} = DIC_o\sigma_{yo}/\sigma_y(t)$. Figure 5-9 shows the average concentration as a function of time traveling downstream from the manifold. The manifold achieves high initial dilution, but it takes a long time to achieve much additional dilution beyond that. A zero solving scheme can be used to get the volume in different pH ranges from Equation 5.7; this yields a volume of about $1.3km^3$ of water between a pH drop of 0.5 and 0.1 after ten hours.

5.4 Summary

Figure 5-10 allows comparison of the three techniques in terms of average pH drop. Generally, the towed pipe and the hydrate plume create the highest initial pH impacts. Both are able to achieve a good level of dilution in the ten hours, although the towed pipe benefits more from the lateral dilution. The sea-floor mounted manifold achieves a low near field pH impact, but doesn't benefit much from lateral dilution due to its large, uniform initial concentration field. Overall, the towed pipe method yields the lowest pH impact after ten hours.

Figure 5-11 shows the volumes in different pH shift ranges for each method. The towed

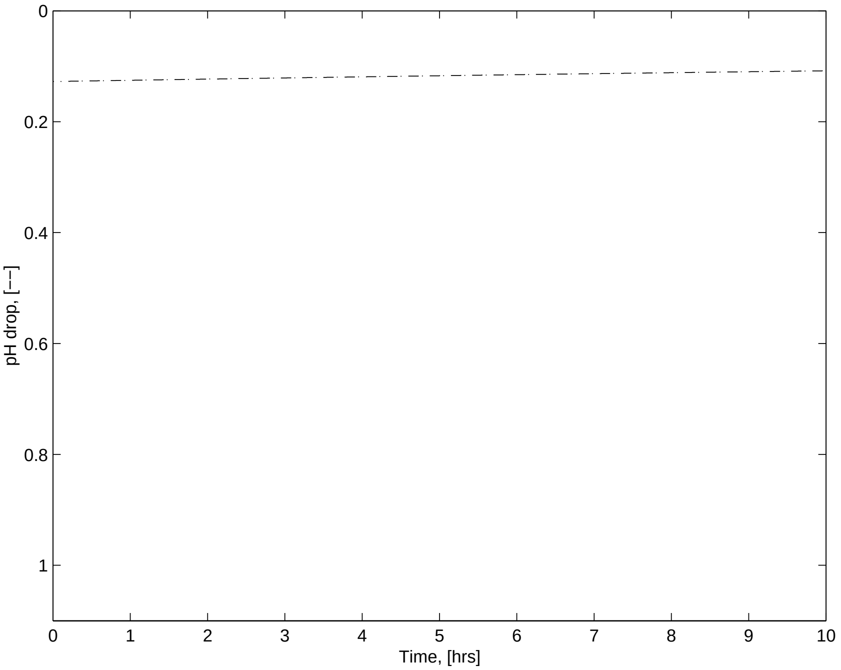

Figure 5-9: pH drop traveling away from a liquid CO_2 manifold as a function of time.

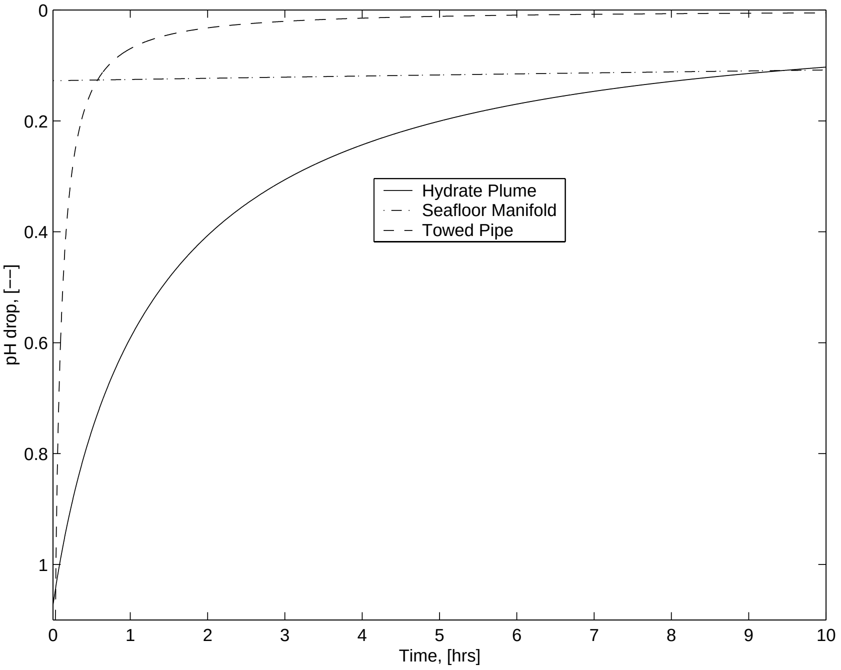

Figure 5-10: pH drop traveling away from different CO_2 releases as a function of time.

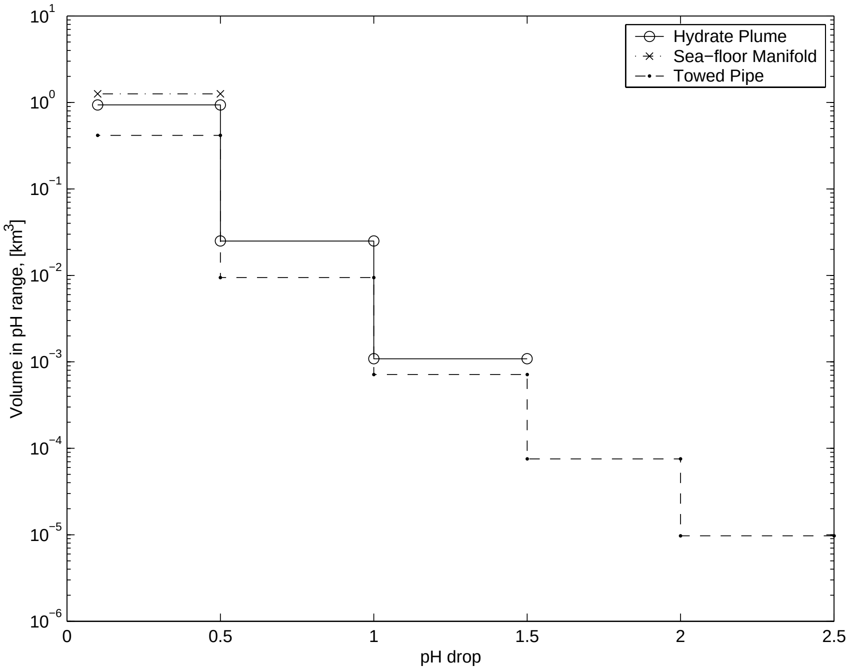

Figure 5-11: Volume of water at different pH drop ranges produced by different CO_2 releases. Plotted points represent pH ranges: $0.1 < \Delta pH < 0.5, 0.5 < \Delta pH < 1.0, 1.0 < \Delta pH < 1.5, 1.5 < \Delta pH < 2.0, \Delta pH > 2.0$.

pipe shows the most potential for acute (high pH shift) impacts due to its low initial mixing. The sea-floor mounted manifold could present a higher danger for chronic impact, based on its large volume in the lowest pH shift range. The hydrate plume represents a compromise between the other two cases.

Overall, this rough analysis indicates that any of the three techniques can achieve reasonable dilution if designed properly. The towed ship technique is the most desirable for reaching ambient pH levels quickly, while the sea-floor manifold provides the best near field dilution.

5.4.1 Importance of Lateral Diffusion

For all three techniques, lateral diffusion is modeled as the dominant process affecting downstream dilution. The amount of dilution provided by lateral diffusion, parameterized after Okubo (1971), depends on both time and the initial size of the concentration field. In other words, as described in Section 4.2.3, $\sigma_y = f(t_o + t)$, where t_o is the equivalent initial time based on the patch size. It follows that for lateral diffusion to be significant, t must be at least of the same order of t_o. It is therefore helpful to compare the magnitudes of the equivalent initial timescales for the three releases.

For the hydrate plume, the initial lateral size is on the order of ten meters. This gives an initial equivalent timescale of about half an hour, indicating that lateral diffusion becomes important rather quickly, as shown above. The towed pipe release as modeled has an initial timescale of zero, and so is impacted by lateral diffusion immediately. Finally, the manifold type release has a initial size on the order of thousands of meters, giving an equivalent initial time scale of about two and a half days. So, it takes a long time for lateral diffusion to provide much dilution of the manifold base release as indicated above.

5.4.2 Sensitivity to Design Variables

The three cases presented above were demonstrated for a selected mass injection rate and nominal values for the other relevant design variables. It is instructive to consider how changes in the design variables might change dilution properties.

Chapter 4 explored in detail the effect of design variables such as mass injection rate for a CO_2 hydrate particle plume. In general, it was shown that increasing particle diameter or decreasing injection rate improved dilution.

Equation 5.6 is the model equation for the downstream dilution of a towed pipe. This simple relation, repeated below for convenience, indicates the relationship between dilution and the design variables $\dot{m}$, h (determined by particle diameter), and U_s. As modeled, the lateral diffusion will be the same regardless of the design variable values.

$$DIC_{avg} = \frac{\dot{m}}{3\sigma_y(t) h U_S} \tag{5.8}$$

Downstream excess DIC increases linearly with $\dot{m}$, and is proportional to the inverse of h and U_s. It follows that increases in $\dot{m}$ can be balanced by increases in the other design variables.

The dilution properties of a manifold release are somewhat different, in that lateral diffusion scales with a slightly different length scale than the initial concentration, as indicated in Equation 5.9 (i.e., the initial lateral size is based on the horizontal length, whereas initial concentration is based on the length of the manifold). Equation 5.9 is an approximation for the average excess DIC once the concentration field produced by the manifold has traveled sufficiently far to have a Gaussian rather than error function shape.

$$DIC_{avg} = \frac{\dot{m}}{hLu_a} \cdot \frac{\sigma_{yo}}{\sigma_y(t)} \tag{5.9}$$

The first multiplicative term, $\frac{\dot{m}}{hLu_a}$, is the predicted nearfield concentration. It indicates that increases in $\dot{m}$ can be offset with increases in h and L (or by finding a region with high ambient current, u_a). Substituting $\sigma_{yo} = h/3\tan\theta$ into Equation 5.9 gives the following relation:

$$DIC_{avg} = \frac{\dot{m}}{Lu_a} \cdot \frac{1}{3\tan\theta\sigma_y(t)}. \tag{5.10}$$

Equation 5.10 indicates the general downstream dilution behavior for a sea-floor manifold. Since $\tan\theta$ is an increasing function of θ up to 90 degrees, a steep sea floor is desirable. The effect of h is effectively canceled out in this formulation, as h acts to decrease downstream dilution but increase initial dilution. The linear dependence on $\dot{m}$ remains, with an inverse proportionality to L and u_a. The design of a manifold with length on the order of thousands of meters has important implication for downstream dilution. As mentioned above, a concentration field of this size will not experience significant dilution for a couple of days. It is therefore important to design a manifold release of this type such that the nearfield concentrations are at levels tolerable for exposure lengths of days.

Chapter 6

Conclusions

6.1 Summary

The properties of CO_2 hydrate plumes were explored using a two-phase integral plume model. The model, presented earlier in Crounse (2000), was updated to function for descending plumes, to include properties relevant to CO_2 hydrates, and to model polydisperse particle releases.

The model was calibrated based on available experimental data. Calibration of fluxes and characteristic plume heights was based on small-scale laboratory data, while the mass transfer model was calibrate based on a small field experiment.

Particle size distribution was found to have some effect on local plume properties, but little effect on integrated properties such as average excess DIC concentration and average intrusion depth.

Average intrusion depth and plume depth were found to increase quite strongly with particle diameter, and noticeably with injection rate. Average excess DIC and pH drop were found to decrease with particle diameter, and increase with injection rate. An increase in injection rate by a factor of 1000 only increased excess DIC by a factor of about 3, indicating a beneficial near field dilution effect with increased injection rate. Far field dilution was found to be more favorable for lower injection rates due to their lower initial volume.

Sensitivity tests indicate a high sensitivity to the mass transfer model, although the trends presented are expected to stay the same. A simple comparison of trap height and separation height in cross flow revealed that some of the low injection rate runs were in the strong current regime. The plume group effect (i.e. characteristic plume depth divided by the depth of an individual particle) was shown to increase with injection rate and decreasing particle size. Moreover, the group effect was shown to be somewhat enhanced for negatively buoyant CO_2 plumes, an effect that also decreased with injection rate.

A comparison of three release methods – a pure hydrate plume, a towed pipe, and a sea-floor mounted manifold – illustrated the relative benefits of initial dilution in the vertical, longitudinal, and lateral directions, respectively. Additionally, modeling of a mound of CO_2 hydrates on the sea-floor indicated pH impacts that were comparable but somewhat larger than those of a pure hydrate plume. The towed pipe release gave initially high pH shifts, but reached ambient levels quickly. The sea-floor manifold release showed high initial dilution with little additional dilution in the far field. The hydrate plume gave somewhat high near field pH shifts with far field values similar to the sea-floor manifold.

6.2 Conclusions

The most notable conclusions are those related to the viability and design of a CO_2 hydrate release in the deep ocean. It is important to remember that the absolute values of quantities such as sequestration depth and pH are highly sensitive to the mass transfer model. However, the relative trends should be considered reliable. The possibility for very deep sequestration is probably the greatest potential advantage of hydrate plumes. This depth is expected to increase with both particle diameter and mass injection rate. The pH drop induced by a hydrate plume is minimized in effect by increasing particle diameter or decreasing mass injection rate. An injection rate of up to $100 kg/s$ in a single plume seems environmentally feasible, though this conclusion is somewhat tenuous until the mass transfer model is better calibrated. As long as a good measure of the mean particle diameter is known, the distribution of particle sizes is not expected to impact integrated plume characteristics significantly.

The comparison of different injection techniques indicates that there are probably many ways to achieve acceptable dilution of CO_2 in the ocean. There may be more of a discrepancy in sequestration depth among different techniques.

6.3 Recommendations for Further Study

As with any modeling effort, the accuracy of the results depends on having good experimental data to calibrate against. To that end, more data is needed on the characteristics of hydrate particles: size, shape, and dissolution rate. Data on multi-phase plumes with particle dissolution is needed as well, to further validate the physical model. Data on polydisperse particles would be useful to validate those results.

Bibliography

Adams, E. E., Caulfield, J. & Zhang, X. Y. (1997), Sinking of a CO_2-enriched gravity current, *in* 'Proc. XXVII IAHR Congress, San Francisco'.

Adams, E. E., Golomb, D., Zhang, X. Y. & Herzog, H. J. (1995), Confined release of CO_2 into shallow sea water, *in* 'Direct Ocean Disposal of Carbon Dioxide', TERRAPUB, Tokyo, pp. 153–164.

Alendal, G. & Drange, H. (2001), 'Two-phase, near field modeling of purposefully released CO_2 in the ocean', *J. Geophysical Research* **106**(C1), 1085–1096.

Asaeda, T. & Imberger, J. (1993), 'Structure of bubble plumes in linearly stratified environments', *J. Fluid Mech.* **249**, 35–57.

Aya, I., Yamane, K. & Narai, H. (1997), 'Solubility of CO_2 and density of CO_2 hydrate at 30 mpa', *Energy* **22**(2/3), 263–271.

Aya, I., Yamane, K. & Shiozaki, K. (1999), 'Proposal of self sinking CO_2 sending system: Cosmos', *Greenhouse Gas Control Technologies* pp. 269–274.

Caldeira, K. & Rau, G. H. (2000), 'Accelerating carbonate dissolution to sequester carbon dioxide in the ocean: Geochemical implications', *Geophysical Research Letters* **27**(2), 225–228.

Caulfield, J. A. (1996), Environmental impacts of carbon dioxide ocean disposal: Plume predictions and time dependent organism experience, MS thesis, Dept. of Civ. Envir. Engrg., MIT, Cambridge, MA.

Chen, B. (2001), A numerical prediction on plume structure of liquid CO_2 in the ocean-a near field model, *in* 'Proc. 5th Int'l Conf. on Greenhouse Gas Control Technologies', pp. 417–422.

Clift, R., Grace, J. R. & Weber, M. E. (1978), *Bubbles, Drops, and Particles*, Academic Press, New York, NY.

Crounse, B. C. (2000), Modeling buoyant droplet plumes in a stratified environment, MS thesis, Dept. of Civ. Env. Engrg., MIT, Cambridge, MA.

Crowe, C. T., Sommerfeld, M. & Tsuji, Y. (1998), *Multiphase flows with droplets and particles*, CRC Press LLC, Boca Raton, FL.

Dickson, A. G. & Goyet, C., eds (1994), *Handbook of Methods for the Analysis of the Various Parameters of the Carbon Dioxide System in Sea Water*, ORNL/CDIAC-74, Department of Energy.

Fujioka, Y., Takeuchi, K., Shindo, Y. & Komiymama, H. (1994), 'Shrinkage of liquidCO_2 droplets in water', *International Journal of Energy Research* **18**, 765–769.

Golomb, D. & Angelopoulos, A. (2001), A benign form of CO_2 sequestration in the ocean. Preprint.

Haugen, P. & Drange, H. (1992), 'Sequestration of CO_2 in the deep ocean by shallow injection', *Nature* **357**(28), 1065–1072.

Herzog, H. & Adams, E. E. (1996), Environmental impacts of ocean disposal of co_2, Technical report, prepared for the U.S. Department of Energy, MIT energy Lab.

Herzog, H., Caldeira, K. & Adams, E. (2001), Carbon sequestration via direct injection, *in* J. Steele, S. Thorpe & K. Turekian, eds, 'Encyclopedia of Ocean Sciences', Vol. 1, Academic Press, London, UK, pp. 408–414.

Herzog, H., Drake, E. & Adams, E. E. (1997), CO_2 capture, reuse and storage technologies for mitigating global climate change, a white paper, Technical report, prepared for the U.S. Department of Energy, MIT energy Lab.

Hirai, S., Okazaki, K., Araki, N., Yazawa, H., Ito, H. & Hijikata, K. (1996), 'Transport phenomena of liquid CO_2 in pressurized water flow with clathrate-hydrate at the interface', *Energy Convers. Mgmt.* **37**(6-8), 1073–1078.

Hirai, S., Okazaki, K., Tabe, Y., Hijikata, K. & Mori, Y. (1997), 'Dissolution rate of liquid CO_2 in pressurized water flows and the effect of clathrate films', *Energy* **22**(2/3), 285–293.

Hirai, S., Tabe, Y., Tanaka, G. & Okazaki, K. (1999), Advanced co_2 ocean dissolution technology for longer term sequestration with minimum biological impacts, *in* P. Riemer, B. Eliasson & A. Wokaun, eds, 'Greenhouse Gas Control Technologies', Elsevier Science Ltd., pp. 317–322.

Holder, G., Mokka, L. & Warzinski, R. (2001), Formation of hydrates from single-phase aqueous solutions and implications for ocean sequestration of CO_2, *in* 'Preprints of Spring 2000 National Meeting in San Diego, CA', ACS Division of Fuel Chemistry.

McDougall, T. J. (1978), 'Bubble plumes in stratified environments', *J. Fluid Mech.* **85**(4), 655–672.

Miller, L. A., Johnson, W. K. & Arychuk, M. (2000), Kona background survey, august 1999. Chemical Data Report: Institute of Ocean Sciences, Canada.

Morel, F. M. M. & Hering, J. G. (1993), *Principles of aquatic chemistry*, Wiley-Interscience.

Mori, Y. H. & Mochizuki, T. (1998), 'Dissolution of liquid CO_2 into water at high pressures: A search for the mechanism of dissolution being retarded through hydrate film formation', *Energy Convers. Mgmt.* **39**(7), 567–568.

Morton, B. R. (1962), 'Coaxial turbulent jets', *J. Heat and Mass Transfer* **5**, 955–965.

Murray, C. N., Visintini, L., Bidoglio, G. & Henry, B. (1996), 'Permanent storage of carbon dioxide in the marine environment: The solid CO_2 penetrator', *Energy Convers. Mgmt* **37**(6-8), 1067–1072.

Nakashiki, N., Ohsumi, T. & Shitashima, K. (1994), Sequestering of CO_2 in a deep ocean, Technical report, Central Research Institute of Electric Power Industry, 1646 Abiko, Abiko-City, Chiba 270-11, Japan.

Okubo, A. (1971), 'Oceanic diffusion diagrams', *Deep Sea Research* **18**, 789–802.

Radhakrishan, R., Demurov, A., Herzog, H. & Trout, B. L. (2001), 'A consistent and verifiable macroscopic model for the dissolution of liquid CO_2 in water under hydrate forming conditions', *Energy Conversion and Management* . Submitted.

Rau, G. H. & Caldeira, K. (1999), 'Enhanced carbonate dissolution: a means of sequestering waste CO_2 as ocean bicarbonate', *Energy Conversion and Management* **40**, 1803–1813.

Rehder, G., Kirby, S. H., Durham, W. B., Stern, L., Peltzer, E. T. & Pinkston, J. (2001), Dissolution rates of synthetic methane hydrate and carbon dioxide hydrate in undersaturated seawater at 1000m depth. Report at MBARI.

Reingold, L. S. (1994), An experimental comparison of bubble and sediment plumes in stratified environments, MS thesis, Dept. of Civ. Env. Engrg., MIT, Cambridge, MA.

Roy, R. N., Roy, L. N., Vogel, K. M., Moore, C. P., Pearson, T., Good, C. E., Millero, F. J. & Campbell, D. M. (1993), 'The dissociation constants of carbonic acid in seawater at salinities 5 to 45 and temperatures 0 to 45 degrees c', *Marine Chemistry* .

Saito, T., Kajishima, T. & Naguosa, R. (2000), 'CO_2 sequestration at sea by gas-lift system of shallow injection and deep releasing', *Environ. Sci. Technol.* **34**, 4140–4145.

Sato, T. & Hama, T. (2001), Numerical simulation of dilution process in CO_2 ocean sequestration, *in* 'Proc. 5th Int'l Conf. on Greenhouse Gas Control Technologies', pp. 475–480.

Schladow, S. G. (1992), 'Bubble plume dynamics in a stratified medium and the implications for water quality amelioration in lakes', *Water Resources Research* **28**(2), 313–321.

Sloan, E. D. (1997), *Clathrate Hydrates of Natural Gases*, Marcel Dekker, New York, NY.

Sloan, E. D. (1998), 'Gas hydrates: Review of physical/chemical properties', *Energy and Fuels* **12**, 191–196.

Socolofsky, S. A. (2001), Laboratory Experiments of Multi-phase Plumes in Stratification and Crossflow, Ph.D. Thesis, Dept. of Civ. Env. Engrg., MIT, Cambridge, MA.

Zeebe, R. E., Wolf-Gladrow, D. A. & Jansen, H. (1999), 'On the time to establish chemical and isotopic equilibrium in the carbon dioxide system', *Marine Chemistry* **65**, 135–153.